JGR Solid Earth

RESEARCH ARTICLE
10.1029/2018JB016596

# An Optimized Short-Arc Approach: Methodology and Application to Develop Refined Time Series of Tongji-Grace2018 GRACE Monthly Solutions

**Qiujie Chen[1,2,3,4], Yunzhong Shen[1], Wu Chen[2], Olivier Francis[3], Xingfu Zhang[5], Qiang Chen[3], Weiwei Li[6], and Tianyi Chen[1]**

[1]College of Surveying and Geo-informatics, Tongji University, Shanghai, China, [2]Department of Land Surveying and Geo-informatics, The Hong Kong Polytechnic University, Hong Kong, [3]Faculté des Science, de la Technologie et de la Communication, University of Luxembourg, Luxembourg, [4]Institute of Geodesy and Geo-information, University of Bonn, Bonn, Germany, [5]Departments of Surveying and Mapping, Guangdong University of Technology, Guangzhou, China, [6]College of Geomatics, Shandong University of Science and Technology, Qingdao, China

**Key Points:**
- The optimized short-arc approach greatly reduces the condition number of the final normal equation for estimating gravity field parameters
- The noise whitening method is able to mitigate the impacts of low-frequency noise in observations on gravity field modeling
- Tongji-Grace2018 monthly models based on the optimized short-arc approach greatly reduce the noise and improve the signal-to-noise ratio

**Correspondence to:**
Y. Shen,
yzshen@tongji.edu.cn

**Citation:**
Chen, Q., Shen, Y., Chen, W., Francis, O., Zhang, X., Chen, Q., et al. (2019). An optimized short-arc approach: Methodology and application to develop refined time series of Tongji-Grace2018 GRACE monthly solutions. *Journal of Geophysical Research: Solid Earth*, *124*. https://doi.org/10.1029/2018JB016596

Received 22 AUG 2018
Accepted 18 MAY 2019
Accepted article online 24 MAY 2019

**Abstract** Considering the unstable inversion of ill-conditioned intermediate matrix required in each integral arc in the short-arc approach presented in Chen et al. (2015, https://doi.org/10.1002/2014JB011470), an optimized short-arc method via stabilizing the inversion is proposed. To account for frequency-dependent noise in observations, a noise whitening technique is implemented in the optimized short-arc approach. Our study shows that the optimized short-arc method is able to stabilize the inversion and eventually prolong the arc length to 6 hr. In addition, the noise whitening method is able to mitigate the impacts of low-frequency noise in observations. Using the optimized short-arc approach, a refined time series of Gravity Recovery and Climate Experiment (GRACE) monthly models called Tongji-Grace2018 has been developed. The analyses allow us to derive the following conclusions: (a) During the analyses over the river basins (i.e., Amazon, Mississippi, Irrawaddy, and Taz) and Greenland, the correlation coefficients of mass changes between Tongji-Grace2018 and others (i.e., CSR RL06, GFZ RL06, and JPL RL06 Mascon) are all over 92% and the corresponding amplitudes are comparable; (b) the signals of Tongji-Grace2018 agree well with those of CSR RL06, GFZ RL06, ITSG-Grace2018, and JPL RL06 Mascon, while Tongji-Grace2018 and ITSG-Grace2018 are less noisy than CSR RL06 and GFZ RL06; (c) clearer global mass change trend and less striping noise over oceans can be observed in Tongji-Grace2018 even only using decorrelation filtering; and (d) for the tests over Sahara, over 36% and 19% of noise reductions are achieved by Tongji-Grace2018 relative to CSR RL06 in the cases of using decorrelation filtering and combined filtering, respectively.

## 1. Introduction

The mass redistributions of the Earth system among atmosphere, ocean, ice sheet, hydrology, and solid Earth inevitably cause time-related variations in the Earth's gravity field (Kusche et al., 2012; Tapley et al., 2004; Wahr et al., 2004). The Gravity Recovery and Climate Experiment (GRACE) mission was launched in March 2002 (Tapley et al., 2004) to measure the variations in the Earth's gravity field at global scale. Though the GRACE mission ended operation last year due to degradation of the batteries, over 15 years of measurements collected by the GRACE mission have brought us unprecedented understanding of the Earth's mass transport processes. Various data processing methods to the GRACE measurements have been developed, resulting in various time-variable gravity field models in terms of unconstrained spherical harmonics (Bettadpur, 2018; Chen et al., 2016; Dahle et al., 2018; Mayer-Gürr et al., 2018; Meyer et al., 2016; Yuan, 2018; Guo & Zhao, 2018; Wang et al., 2015), regularized or filtered spherical harmonics (Farahani et al., 2017; Lemoine et al., 2018), and mascon grids (Luthcke et al., 2013; Save et al., 2016; Watkins et al., 2015). As the traditional and established representation of gravity field solutions, the spherical harmonic models are usually applied to most of geophysical signal analyses (Chen et al., 2014; Schumacher et al., 2018; Velicogna & Wahr, 2013).

Through over 15 years of efforts, numerous research teams have greatly improved the GRACE gravity field models by developing various refined data processing methods. The improved data processing algorithms generally focus on refinements of background force models, GRACE Level-1b data, gravity field recovery methodologies and noise modeling. Imperfectness of the background force models (especially ocean tide

and dealiasing models; Daras & Pail, 2017;Zenner et al., 2012) will inevitably cause temporal aliasing, which is one of the reasons for the north-south stripes (Loomis et al., 2012; Wiese et al., 2011). The enhanced ocean tide modeling (Mayer-Gürr et al., 2012) and nontidal dealiasing strategy (Flechtner & Dobslaw, 2013) were demonstrated to reduce the impact of temporal aliasing on gravity field estimates to some extent. The GRACE Level-1b data processed by the Jet Propulsion Laboratory (JPL) have matured from RL01 to RL03, where every new version of GRACE Level-1b data consistently brought clear improvement on gravity field estimates (Chambers & Bonin, 2012; Dahle et al., 2014; Dahle et al., 2018). During gravity field determination, the gravity field modeling approaches (e.g., dynamic approach, short-arc approach and its modified version, acceleration approach, celestial mechanics approach, and energy balance one) and noise modeling (random noise and frequency-dependent noise modeling) are of great importance for improving the GRACE solutions.

For the well-known short-arc approach, it was first established by Schneider (1968) for orbit determination and then applied by Mayer-Gürr (2006) to derive several high-quality gravity field models. Before solving gravity field parameters, this approach needs to use a priori gravity field models to correct orbits when computing gravitational force acting on satellites. A modified short-arc approach that simultaneously estimates the orbit corrections and gravity field parameters was therefore proposed by Chen et al. (2015). Consequently, the modified short-arc method becomes insensitive toward the a priori gravity field information. Using the proposed method, Chen et al. (2015) developed the Tongji-GRACE01 monthly solutions that are comparable to the official GRACE RL05 models. Recently, a further enhancement was implemented for the modified short-arc method to model the errors of accelerometer measurement and attitude data (Chen et al., 2016), leading to clear noise reductions in the derived Tongji-GRACE02 monthly solutions. However, there is still some space to further improve the modified short-arc method. In principle, long-arc techniques are more sensitive to long-term variations in the Earth's gravity field (Cheng et al., 1997) and contributes better estimates of tesseral harmonic coefficients (Taff, 1985). Moreover, long arcs probably amplify those minor forces acting on spacecraft (Xu, 2008), which means that these signals are more likely to be captured. However, the arc length used in the modified short-arc approach is generally 2 hr (Chen et al., 2015; Shen et al., 2015), which is still significantly shorter than those used in either the dynamic approach (1-day arcs; Bettadpur, 2012; Dahle et al., 2012; Watkins & Yuan, 2014) or acceleration approach (6-hr arcs; Ditmar & van der Sluijs, 2004; Liu et al., 2010). One may discuss whether it is possible to further extend the arc length in the modified short-arc approach and what the practical contribution to gravity field quality is. One of the reasons for limiting the arc length in the modified short-arc method is that the stability of inversing an intermediate matrix is decreased along with the increase of arc length. To briefly explain it, we write the observation equation for both orbits and range rates in the modified short-arc method as $\boldsymbol{C}\,\boldsymbol{x}+\boldsymbol{D}\,\boldsymbol{v}=\boldsymbol{y}$ for any arc ($\boldsymbol{x}$ and $\boldsymbol{v}$: parameters and observation corrections; $\boldsymbol{C}$ and $\boldsymbol{D}$: design matrices for $\boldsymbol{x}$ and $\boldsymbol{v}$; $\boldsymbol{y}$ is residual vector). The inversion of the intermediate matrix ($\boldsymbol{DQD}^{\boldsymbol{T}}$; $\boldsymbol{Q}$ is variance-covariance matrix of observations) should be computed in each arc before generating subnormal equation for this arc, whose condition number will increase rapidly when prolonging the arc length. In other words, stabilizing the inversion would allow to further extend the arc length. However, until now, nearly no research was conducted on exploring any possibility to extend the arc length in the modified short-arc method by stabilizing the inversion.

Noise modeling is also worth noting in gravity field estimation. Especially for K-band range rate measurements, many studies have shown that such measurements are dominated by frequency-dependent noise (Farahani et al., 2013; Mayer-Gürr et al., 2014). Ditmar et al. (2012) pointed out that the frequency-dependent noise in the observations is severely corrupted by the errors in the GRACE orbits. Hence, different noise modeling strategies were applied by various research centers. To account for the effects of the frequency-dependent noise in the observations on gravity field modeling, empirical parameters are generally introduced (Liu et al., 2010; Zhao et al., 2011; Zhou et al., 2017). The frequency-dependent noise can also be suppressed by frequency-dependent data weighting (FDDW) techniques (Farahani et al., 2017; Guo et al., 2018; Klees & Ditmar, 2004). However, most processing centers do not consider the FDDW and less often discuss the noise behaviors of orbit measurements. One possible reason for that is many approaches do not use orbits as observations for the estimation of the geopotential coefficients. Even though the contribution of the orbit measurements to gravity field estimates is limited to the low degrees, the orbits are of importance for processing the K-band data. Since any kind of orbits (dynamic, reduced-dynamic, or kinematic

orbits) is dominated by the significant frequency-dependent noise, much more work should be carried out to analyze and model the noise.

To enhance gravity field solutions, this research proposes an optimized short-arc approach by stabilizing the inversion of intermediate matrix and modeling the frequency-dependent noise. Using the optimized method, a new time series of GRACE monthly solutions called Tongji-Grace2018 (with maximum degree and order of both 60 and 96) for the period April 2002 to August 2016 are developed by Tongji University. The rest of paper is outlined as follows. The theoretical model for the optimized short-arc approach is presented in section 2. In section 3, it shows the frequency-dependent noise modeling and discusses the stabilities of the short-arc method proposed by Chen et al. (2015) and the optimized one. The detailed data processing procedures for Tongi-Grace2018 monthly models are given in section 4. Sections 5 and 6 are left for discussions on Tongi-Grace2018 in terms of noise and signal levels. Conclusions are drawn in section 7.

## 2. Methodology

### 2.1. Functional Model for the Optimized Short-Arc Approach

For an arc with $N$+1 kinematic orbit measurements $\boldsymbol{r}(\tau_k)(k = 0,1, \ldots ,N)$, the observation equations at boundary epochs are

$$\mathbf{r}(\tau_0) + \mathbf{v}_\mathbf{r}(\tau_0) = \mathbf{r}_0 + \delta\mathbf{r}_0 \tag{1}$$

$$\mathbf{r}(\tau_N) + \mathbf{v}_\mathbf{r}(\tau_N) = \mathbf{r}_N + \delta\mathbf{r}_N \tag{2}$$

where $\boldsymbol{v_r}(\tau_i)\,(i = 0,N)$ is the corrections to position measurements at the boundary epochs; $\delta\boldsymbol{r}_0$ and $\delta\boldsymbol{r}_N$ denote the corrections to the boundary position parameters ($\boldsymbol{r}_0$ and $\boldsymbol{r}_N$) to be estimated. For the epochs except for the two boundary epochs, we have position observation equation below:

$$\boldsymbol{r}(\tau_i) + \boldsymbol{v}_r(\tau_i) = \boldsymbol{r}^0(\tau_i) + \delta\boldsymbol{r}^0(\tau_i), i = 1, 2..., N-1. \tag{3}$$

To generate velocity vector at any epoch, the following equation is subsequently given:

$$\dot{\boldsymbol{r}}(\tau_i) = \dot{\boldsymbol{r}}^0(\tau_i) + \delta\dot{\boldsymbol{r}}^0(\tau_i), i = 0, 1..., N. \tag{4}$$

In equations (3) and (4), $\boldsymbol{v_r}(\tau_i)$ is the corrections to the position measurements at normalize time $\tau_i$; $\boldsymbol{r}^0(\tau_i)$ and $\dot{\boldsymbol{r}}^0(\tau_i)$ are the reference position and velocity vectors numerically integrated by $\boldsymbol{r}(\tau_i)$ and a priori parameters (including gravity field coefficients, accelerometer and boundary parameters) and background force models; and $\delta\boldsymbol{r}^0(\tau_i)$ and $\delta\dot{\boldsymbol{r}}^0(\tau_i)$ represent the corrections caused by position measurement errors and insufficient accuracies in the a priori parameters. Before computing the reference position and velocity vectors, we define the a priori values $\boldsymbol{u_0}$ and $\boldsymbol{p_0}$ for the gravity field parameters and accelerometer parameters, respectively. Following the discretization technique presented in Chen et al. (2015), the reference position and velocity vectors can be expressed as a combination of the kinematic orbit measurements in the whole arc by using integration coefficients $\alpha_k$ and $\beta_k$:

$$\boldsymbol{r}^0(\tau_i) = (1-\tau_i)\boldsymbol{r}_0 + \tau_i\boldsymbol{r}_N - T^2\sum_{k=0}^{N}\alpha_k K(\tau_i,\tau_k)\boldsymbol{a}(\boldsymbol{r}_k,\boldsymbol{u}_0,\boldsymbol{p}_0), \tag{5}$$

$$\dot{\boldsymbol{r}}^0(\tau_i) = \frac{\boldsymbol{r}_N-\boldsymbol{r}_0}{T} + T\sum_{k=0}^{N}\beta_k\frac{\partial K(\tau_i,\tau_k)}{\partial\tau_\mathrm{i}}\boldsymbol{a}(\boldsymbol{r}_k,\boldsymbol{u}_0,\boldsymbol{p}_0), \tag{6}$$

where $K$ is the integral kernel for the arc of length $T$ (Chen et al., 2015; Mayer-Gürr, 2006) and $\boldsymbol{a}$ is the a priori force acting on spacecraft. Using the same discretization method, the corrections to the reference position and velocity vectors are subsequently given as

$$\delta \boldsymbol{r}^0(\tau_i) = (1-\tau_i)\delta \boldsymbol{r}_0 + \tau_i \delta \boldsymbol{r}_N - T^2 \sum_{k=0}^{N} \alpha_k K(\tau_i, \tau_k) \left( \frac{\partial \boldsymbol{a}(\boldsymbol{r}_k, \boldsymbol{u}_0, \boldsymbol{p}_0)}{\partial \boldsymbol{u}} \delta \boldsymbol{u} + \frac{\partial \boldsymbol{a}(\boldsymbol{r}_k, \boldsymbol{u}_0, \boldsymbol{p}_0)}{\partial \boldsymbol{p}} \delta \boldsymbol{p} + \frac{\partial \boldsymbol{a}(\boldsymbol{r}_k, \boldsymbol{u}_0, \boldsymbol{p}_0)}{\partial \boldsymbol{r}_k} \boldsymbol{v}_r(\tau_k) \right), \tag{7}$$

$$\delta \dot{\boldsymbol{r}}^0(\tau_i) = \frac{\delta \boldsymbol{r}_N - \delta \boldsymbol{r}_0}{T} + T \sum_{k=0}^{N} \beta_k \frac{\partial K(\tau_i, \tau_k)}{\partial \tau_i} \left( \frac{\partial \boldsymbol{a}(\boldsymbol{r}_k, \boldsymbol{u}_0, \boldsymbol{p}_0)}{\partial \boldsymbol{u}} \delta \boldsymbol{u} + \frac{\partial \boldsymbol{a}(\boldsymbol{r}_k, \boldsymbol{u}_0, \boldsymbol{p}_0)}{\partial \boldsymbol{p}} \delta \boldsymbol{p} + \frac{\partial \boldsymbol{a}(\boldsymbol{r}_k, \boldsymbol{u}_0, \boldsymbol{p}_0)}{\partial \boldsymbol{r}_k} \boldsymbol{v}_r(\tau_k) \right). \tag{8}$$

Both position and velocity vectors of GRACE A and GRACE B are used to form the following observation equation for the K-band range rate measurements:

$$\boldsymbol{F}(\boldsymbol{r}_A(\tau_i), \boldsymbol{r}_B(\tau_i), \boldsymbol{u}, \boldsymbol{p}_A, \boldsymbol{p}_B) = (\boldsymbol{r}_B(\tau_i) - \boldsymbol{r}_A(\tau_i))^T \cdot (\dot{\boldsymbol{r}}_B(\tau_i) - \dot{\boldsymbol{r}}_A(\tau_i))/\rho(\tau_i) \tag{9}$$

in which the symbols A and B indicate GRACE A and GRACE B separately and $\rho(\tau_i)$ is the intersatellite range. We substitute equations from (1) to (8) into the observation equation (9) and carry out the linearization of the observation equation (9), leading to the linearized observation equation for the range rate measurements:

$$\dot{\rho}(\tau_i) + v_{\dot{\rho}}(\tau_i) = \boldsymbol{F}^0 + \frac{\partial \boldsymbol{F}}{\partial \boldsymbol{u}} \delta \boldsymbol{u} + \frac{\partial \boldsymbol{F}}{\partial \boldsymbol{r}_0^{\mathrm{A}}} \delta \boldsymbol{r}_0^{\mathrm{A}} + \frac{\partial \boldsymbol{F}}{\partial \boldsymbol{r}_{\mathrm{N}}^{\mathrm{A}}} \delta \boldsymbol{r}_{\mathrm{N}}^{\mathrm{A}} + \frac{\partial \boldsymbol{F}}{\partial \boldsymbol{r}_0^{\mathrm{B}}} \delta \boldsymbol{r}_0^{\mathrm{B}} + \frac{\partial \boldsymbol{F}}{\partial \boldsymbol{r}_{\mathrm{N}}^{\mathrm{B}}} \delta \boldsymbol{r}_{\mathrm{N}}^{\mathrm{B}} + \frac{\partial \boldsymbol{F}}{\partial \boldsymbol{p}_A} \delta \boldsymbol{p}_A + \frac{\partial \boldsymbol{F}}{\partial \boldsymbol{p}_B} \delta \boldsymbol{p}_B + \sum_{k=0}^{N} \left( \frac{\partial \boldsymbol{F}}{\partial \boldsymbol{r}_{A_k}} v_{r_A}(\tau_k) + \frac{\partial \boldsymbol{F}}{\partial \boldsymbol{r}_{B_k}} v_{r_B}(\tau_k) \right) \tag{10}$$

in which the reference range rate $\boldsymbol{F}^0$ is directly computed from the reference position and velocity vectors; $\delta \boldsymbol{p}_s$ and $\boldsymbol{v}_{r_s}(s = A, B)$ are the corrections to the accelerometer parameters for both satellites and orbit measurements of both satellites, respectively; $\boldsymbol{v}_{\dot{\rho}}$ stands for the corrections to the intersatellite range rate measurements $\dot{\rho}(\tau_i)$; and $\delta \boldsymbol{r}_k^s (k = 0, N; s = A, B)$ represents the corrections to the boundary parameters for both satellites.

### 2.2. Separating Orbits From Range Rate in Constructing Normal Equation

For brevity, the observation equations (1) and (3) for the orbits of both satellites at the $j$th arc ($j$ = 1,2, ... ,$K$) can be rewritten in the form of matrices:

$$\boldsymbol{C}_j^A \boldsymbol{x}_j + \boldsymbol{D}_j^A \boldsymbol{v}_j^A = \boldsymbol{y}_j^A, \tag{11}$$

$$\boldsymbol{C}_j^B \boldsymbol{x}_j + \boldsymbol{D}_j^B \boldsymbol{v}_j^B = \boldsymbol{y}_j^B, \tag{12}$$

where $\boldsymbol{C}_j^s$ and $\boldsymbol{D}_j^s$ ($s = A,B$) stand for partial derivative matrices with respect to the parameters to be estimated $\boldsymbol{x}_j = \left( \delta \boldsymbol{\mu}^T, \delta \boldsymbol{p}_{Aj}^T, \delta \boldsymbol{p}_{Bj}^T, \delta \boldsymbol{r}_{0j}^A T, \delta \boldsymbol{r}_{Nj}^A T \delta \boldsymbol{r}_{0j}^B T, \delta \boldsymbol{r}_{Nj}^B T \right)^T$ and orbit correction vector $\boldsymbol{v}_j^s (s = A, B)$, respectively, as given in the observation equations from (1) to (3); the residual vector $\boldsymbol{y}_j^s$ ($s = A,B$) is formed by subtracting the kinematic orbit measurements from the reference orbit positions. Analogously, the simplified form of the observation equation (10) for the intersatellite range rates is given as follows:

$$\boldsymbol{C}_j^{\dot{\rho}} \boldsymbol{x}_j + \boldsymbol{D}_j^{\dot{\rho}A} \boldsymbol{v}_j^A + \boldsymbol{D}_j^{\dot{\rho}B} \boldsymbol{v}_j^B - \boldsymbol{v}_j^{\dot{\rho}} = \boldsymbol{y}_j^{\dot{\rho}} \tag{13}$$

in which $\boldsymbol{C}_j^{\dot{\rho}}$ and $\boldsymbol{D}_j^{\dot{\rho}s}$ ($s = A,B$) are the partial derivative matrices with respect to the unknown parameters and orbit corrections separately; $\boldsymbol{y}_j^{\dot{\rho}}$ indicates residual vector for range rate measurements. Before further conducting derivation for the above observation equations, we assume there are $N$+1 kinematic orbit measurements and $L$ intersatellite observations at the $j$th arc. Unlike the modified short-arc approach that does not treat boundary vectors as parameters, we can derive $N$+1 orbit observation equations for either GRACE A or GRACE B because boundary parameters are introduced when forming observation equations. This means that $\boldsymbol{D}_j^A$ and $\boldsymbol{D}_j^B$ for both satellites become square matrices with full rank, so they are invertible. We

therefore multiply equations (11) and (12) by $\left(\boldsymbol{D}_j^A\right)^{-1}$ and $\left(\boldsymbol{D}_j^B\right)^{-1}$ separately, leading to more concise observation equations for both orbits as follows:

$$\mathbf{v}_j^A = \left(-\left(\mathbf{D}_j^A\right)^{-1}\mathbf{C}_j^A\right)\mathbf{x}_j - \left(-\left(\mathbf{D}_j^A\right)^{-1}\mathbf{y}_j^A\right) \tag{14}$$

$$\mathbf{v}_j^B = \left(-\left(\mathbf{D}_j^B\right)^{-1}\mathbf{C}_j^B\right)\mathbf{x}_j - \left(-\left(\mathbf{D}_j^B\right)^{-1}\mathbf{y}_j^B\right) \tag{15}$$

Here we define

$$\overline{\mathbf{C}}_j^A = \left(-\left(\mathbf{D}_j^A\right)^{-1}\mathbf{C}_j^A\right); \quad \overline{\mathbf{y}}_j^A = \left(-\left(\mathbf{D}_j^A\right)^{-1}\mathbf{y}_j^A\right) \tag{16}$$

$$\overline{\mathbf{C}}_j^B = \left(-\left(\mathbf{D}_j^B\right)^{-1}\mathbf{C}_j^B\right); \quad \overline{\mathbf{y}}_j^B = \left(-\left(\mathbf{D}_j^B\right)^{-1}\mathbf{y}_j^B\right) \tag{17}$$

$$\overline{\boldsymbol{C}}_j^{\dot{\rho}} = \boldsymbol{C}_j^{\dot{\rho}} + \boldsymbol{D}_j^{\dot{\rho}A}\overline{\boldsymbol{C}}_j^A + \boldsymbol{D}_j^{\dot{\rho}B}\overline{\boldsymbol{C}}_j^B; \overline{\boldsymbol{y}}_j^{\dot{\rho}} = \boldsymbol{y}_j^{\dot{\rho}} + \boldsymbol{D}_j^{\dot{\rho}A}\overline{\boldsymbol{y}}_j^A + \boldsymbol{D}_j^{\dot{\rho}B}\overline{\boldsymbol{y}}_j^B. \tag{18}$$

Based on the definitions (16) and (17), the orbit observation equations for GRACE A and GRACE B can be further simplified as

$$\mathbf{v}_j^A = \overline{\mathbf{C}}_j^A\mathbf{x}_j - \overline{\mathbf{y}}_j^A \tag{19}$$

$$\mathbf{v}_j^B = \overline{\mathbf{C}}_j^B\mathbf{x}_j - \overline{\mathbf{y}}_j^B \tag{20}$$

Taking equations from (18) to (20) and (13) into account, we derive a more concise observation equation for the range rate measurements as follows:

$$\boldsymbol{v}_j^{\dot{\rho}} = \overline{\boldsymbol{C}}_j^{\dot{\rho}}\boldsymbol{x}_j - \overline{\boldsymbol{y}}_j^{\dot{\rho}}. \tag{21}$$

Finally, the subnormal equation at the $j$th arc can be formed as

$$\sum_{s=A,B,\dot{\rho}}\left(\overline{\boldsymbol{C}}_j^s\right)^T\left(\boldsymbol{Q}_j^s\right)^{-1}\left(\overline{\boldsymbol{C}}_j^s\right)\boldsymbol{x}_j = \sum_{s=A,B,\dot{\rho}}\left(\overline{\boldsymbol{C}}_j^s\right)^T\left(\boldsymbol{Q}_j^s\right)^{-1}\overline{\boldsymbol{y}}_j^s, \tag{22}$$

where $\boldsymbol{Q}_j^s(s = A, B, \dot{\rho})$ denotes the variance-covariance matrices for orbits and intersatellite range rates. As shown in equation (22), the contribution of each observable (orbit of each satellite or intersatellite range rate) to generating normal equation is easy to be assessed. According to equation (22), we generate the subnormal equation for each arc. In this study, the boundary parameters are estimated per arc and accelerometer parameters (scales and biases) are solved per day. The boundary parameters can be first eliminated after generating the subnormal equation for each arc. Once generating the daily normal equation, the accelerometer parameters will also be eliminated immediately. The combination of all the reduced daily normal equations leads to the final monthly normal equation only regarding the geopotential coefficients to be estimated.

### 2.3. Theoretical Merits of the Optimized Short-Arc Method

Before discussing the metrics of the optimized short-arc approach, we need to review the basic formulas for the previous modified short-arc approach (Chen et al., 2015) and explain the corresponding drawback. One of the major distinctions between the functional models of the optimized short-arc approach and the modified one is the parameterization of the boundary epochs. In the modified short-arc approach, the boundary values are directly expressed as kinematic orbit measurements at the boundary epochs plus corrections; thereby, no boundary parameter is introduced. In such a case, the observation equations (1) and (2) are not applicable anymore, indicating that the design matrix $\boldsymbol{D}_j^s$ ($s = A,B$) for kinematic orbit corrections at

the $j$th arc becomes a $m$-by-$n$ irreversible matrix ($m = 3 \times (N-1)$,$n = 3 \times (N+1)$). Consequently, as given in Chen et al. (2015), the observation equations for the pair of orbits and range rates at the $j$th arc along with the corresponding subnormal equation can be summarized as follows:

$$\mathbf{C}_j\mathbf{x}_j + \mathbf{D}_j\mathbf{v}_j = \mathbf{y}_j \tag{23}$$

$$\left(\mathbf{C}_j^T\left(\mathbf{D}_j\mathbf{Q}_j\mathbf{D}_j^T\right)^{-1}\mathbf{C}_j\right)\mathbf{x}_j = \mathbf{C}_j^T\left(\mathbf{D}_j\mathbf{Q}_j\mathbf{D}_j^T\right)^{-1}\mathbf{y}_j,\ \ j = 1, 2, ..., K \tag{24}$$

where

$$\mathbf{C}_\mathrm{j} = \begin{pmatrix} \mathbf{C}_\mathrm{j}^\mathrm{A} \\ \mathbf{C}_\mathrm{j}^\mathrm{B} \\ \mathbf{C}_\mathrm{j}^{\dot{\rho}} \end{pmatrix}; \mathbf{D}_\mathrm{j} = \begin{pmatrix} \mathbf{D}_\mathrm{j}^\mathrm{A} & \mathbf{0} & \mathbf{0} \\ \mathbf{0} & \mathbf{D}_\mathrm{j}^\mathrm{B} & \mathbf{0}\ \mathbf{D}_\mathrm{j}^{\dot{\rho}}\mathrm{B}-\mathbf{I} \\ \mathbf{D}_\mathrm{j}^{\dot{\rho}}\mathrm{A} & & \end{pmatrix},$$

$$\mathbf{y}_\mathrm{j} = \begin{pmatrix} \mathbf{y}_\mathrm{j}^\mathrm{A} \\ \mathbf{y}_\mathrm{j}^\mathrm{B} \\ \mathbf{y}_\mathrm{j}^{\dot{\rho}} \end{pmatrix}; \mathbf{Q}_\mathrm{j} = \begin{pmatrix} \mathbf{Q}_\mathrm{j}^\mathrm{A} & \mathbf{0} & \mathbf{0} \\ \mathbf{0} & \mathbf{Q}_\mathrm{j}^\mathrm{B} & \mathbf{0} \\ \mathbf{0} & \mathbf{0} & \mathbf{Q}_\mathrm{j}^{\dot{\rho}} \end{pmatrix}.$$

Unfortunately, $\boldsymbol{D}_j$ is such an irreversible matrix that we cannot separate equation (23) for each GRACE observable (orbit of each satellite or intersatellite range rate) in the form of equations (19) to (21). In the modified short-arc approach, the large-scale intermediate matrix $\left(\boldsymbol{D}_j\boldsymbol{Q}_j\boldsymbol{D}_j^T\right)$ with dimension generally between 6 and 7 times the arc length should be inversed prior to creating the normal equation, which means that extending arc length will rapidly increase the dimension of this matrix. From the perspective of numerical computation, the large-scale matrix in general makes it more difficult to obtain a stable inversion $\left(\boldsymbol{D}_j\boldsymbol{Q}_j\boldsymbol{D}_j^T\right)^{-1}$, which is the main reason for preventing the extension of the arc length in the modified short-arc method. On the other hand, in the case of the optimized short-arc approach, we only need to individually compute the inversion of matrix $\boldsymbol{D}_j^s(\mathrm{s} = \mathrm{A}, \mathrm{B})$ for each satellite before creating the normal equations, whose dimensions are only triple of the arc length, making it possible to prolong the arc length. Further discussions about the difference of stability between the modified and optimized short-arc methods will be given in section 3.3.

## 3. Discussions on the Optimized Short-Arc Method

### 3.1. Constructing Variance-Covariance Matrices

As stated before, the intersatellite range rate measurements are contaminated by the frequency-dependent noise, and many methodologies have been applied to account for them. One of the methodologies is to construct variance-covariance matrices for the observations. Based on autocovariance or cross-covariance of postfit residuals, different variance-covariance matrices for observations were established under various assumptions (Koch et al., 2010). In this study, a noise whitening technique is applied to construct the variance-covariance matrices for measurements, which is similar to FDDW technique (Farahani et al., 2017) in spite of the difference of detailed implementation between these two techniques. It is necessary to investigate the behavior of the postfit residuals of GRACE measurements before our variance-covariance matrices are created. As an example, we select November 2014 to show the postfit residuals of GRACE measurements derived by using the data processing presented in Chen et al. (2015). Note that the corresponding monthly gravity field model up to degree and order 60 was determined before calculating the residuals. During gravity field modeling, the GRACE measurements (range rates, nongravitational accelerations, and attitudes) from JPL and kinematic orbits computed by Graz University of Technology were used.

As presented in Figure 1, the postfit residuals of orbit and range rate measurements on 15 November 2014 show clear frequency dependency, as illustrated by the power spectrum densities (PSDs) plotted in Figure 2. From Figure 2, it can be seen that both orbit and range rate measurements (especially the orbit

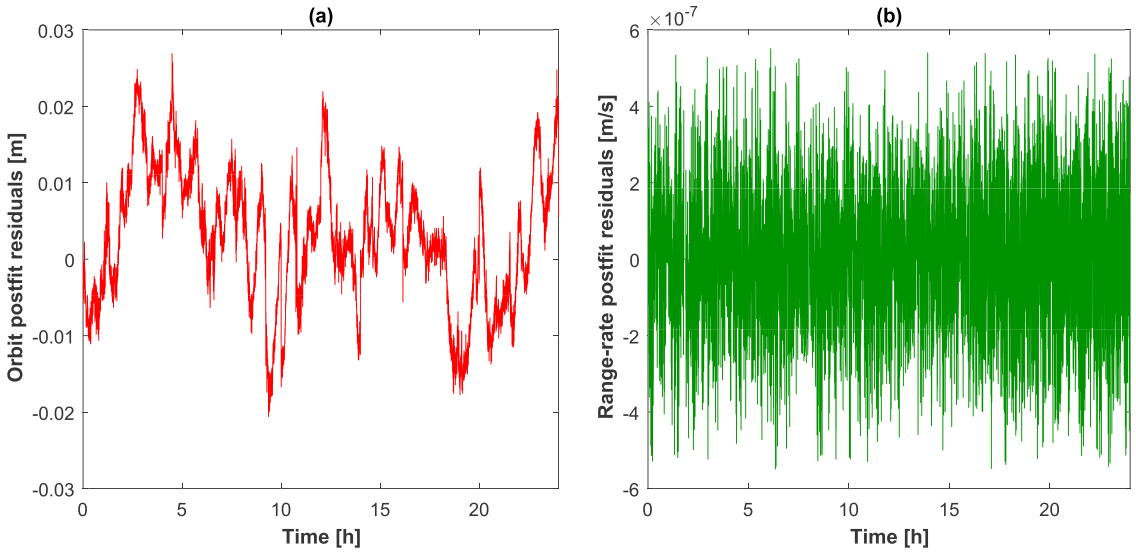


**Figure 1.** Postfit residuals of orbit (a) and range rate (b) measurements on 15 November 2014.

data) are dominated by the low-frequency noise. For the case of range rates, the frequency-dependent noise is usually accounted for via either estimating periodic parameters or introducing variance-covariance matrices. As stated in the introduction, the frequency-dependent noise in the observations is greatly attributed to the errors in GRACE orbits (Ditmar et al., 2012). Due to the imperfect background models used to account for tidal and nontidal variations in both ocean and atmosphere during gravity field modeling (Kurtenbach et al., 2009; Seo et al., 2008), temporal aliasing errors will inevitably propagate to the orbit and K-band observations. This is one of the possible reasons for the frequency-dependent amplitude of the orbit residuals as displayed in Figure 1a, indicating modeling frequency-dependent noise for orbits is theoretically necessary. In this paper, the variance-covariance matrices for orbit and range rate data are constructed rather than doing so only in the range rates (Guo et al., 2018).

Before constructing the variance-covariance matrix $\boldsymbol{Q}_j^s(s = A, B, \dot{\rho})$ in the $j$th arc, we define the frequency-dependent noise for the orbit and intersatellite range rate measurements as $\boldsymbol{e}_j^s(s = A, B, \dot{\rho})$. Applying noise whitening operation, the frequency-dependent noise will become Gaussian white noise $\overline{\boldsymbol{e}}_j^s(s = A, B, \dot{\rho})$:

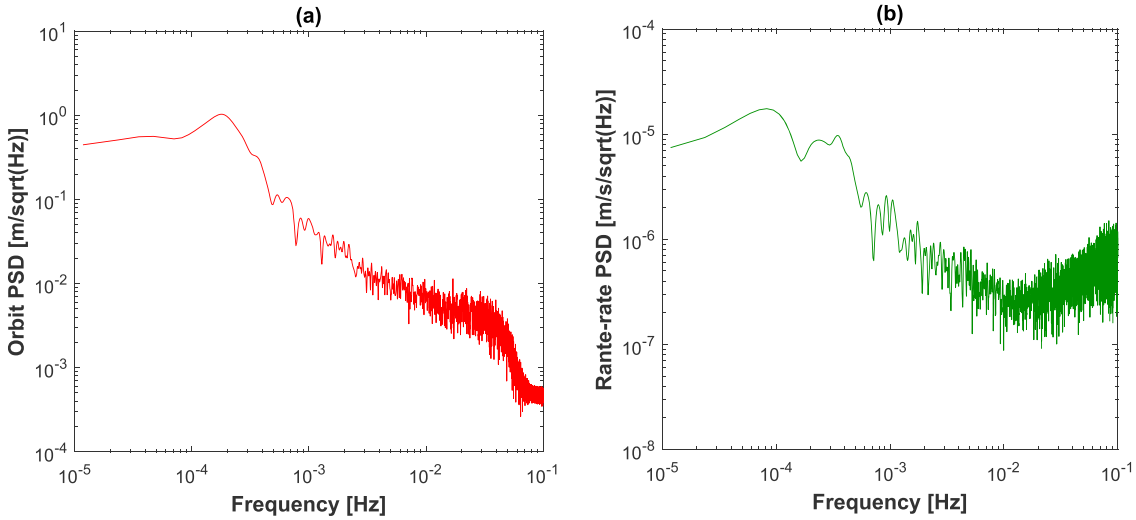


**Figure 2.** Power spectrum densities for orbit (a) and range rate (b) residuals.

**Table 1**
*Computational Schemes*

| Gravity filed solution | Method | Variance-covariance matrix |
|---|---|---|
| Case 1: Md | modified short-arc | diagonal |
| Case 2: Od | optimized short-arc | diagonal |
| Case 3: Mf | modified short-arc | full |
| Case 4: Of | optimized short-arc | full |

*Note.* M = modified; O = optimized; d = diagonal matrices; f = full matrices.

$$\bar{\mathbf{e}}_j^s = \mathbf{H}_j^s \mathbf{e}_j^s \tag{25}$$

where the noise whitening matrix $\boldsymbol{H}_j^s\ (s = A, B, \dot{\rho})$ and the variance of white noise $\bar{\sigma}_j^s (s = A, B, \dot{\rho})$ can be obtained based on the autoregressive (AR) noise model implemented in the ARMASA toolbox (Broersen, 2000; e.g., ARMASA toolbox offered in the MATLAB Central, https://nl.mathworks.com/matlabcentral/fileexchange/1330-armasa). In ARMASA, the AR noise model can be determined by using the Levinson-Durbin algorithm (Broersen & Wensink, 1998). Based on $\bar{\sigma}_j^s (s = A, B, \dot{\rho})$ and the predefined variance of unit weight $\sigma_0$ (it is 2 cm in this study since this value is close to the root-mean-square (RMS) of the postfit residuals of kinematic orbits), the variance-covariance matrix $\bar{\mathbf{Q}}_j^s\ (s = A, B, \dot{\rho})$ for white noise is constructed in the following:

$$\bar{\mathbf{Q}}_j^s = \mathrm{diag}\left[ {(\sigma_j^s)^2} \Big/ {(\sigma_0)^2} \right] \tag{26}$$

According to the law of variance-covariance propagation, we build the relationship between the variance-covariance matrices $\bar{\mathbf{Q}}_j^s (s = A, B, \dot{\rho})$ and $\mathbf{Q}_j^s (s = A, B, \dot{\rho})$ as follows:

$$\bar{\mathbf{Q}}_j^s = \mathbf{H}_j^s \mathbf{Q}_j^s \left( \mathbf{H}_j^s \right)^T \tag{27}$$

Because the whitening matrix $\boldsymbol{H}_j^s (s = A, B, \dot{\rho})$ is invertible, the variance-covariance matrix $\boldsymbol{Q}_j^s (s = A, B, \dot{\rho})$ for the frequency-dependent noise is easily obtained through applying the inversion of $\boldsymbol{H}_j^s$ to both sides of equation (27):

$$\mathbf{Q}_j^s = \left( \mathbf{H}_j^s \right)^{-1} \bar{\mathbf{Q}}_j^s \left( \left( \mathbf{H}_j^s \right)^{-1} \right)^T \tag{28}$$

As the frequency-dependent noise $\boldsymbol{e}_j^s (s = A, B, \dot{\rho})$ for measurements is practically unknown, the variance-covariance matrices $\boldsymbol{Q}_j^s (s = A, B, \dot{\rho})$ for measurements are usually computed on the basis of the postfit residuals of measurements.

### 3.2. Added Value of Optimized Short-Arc Method

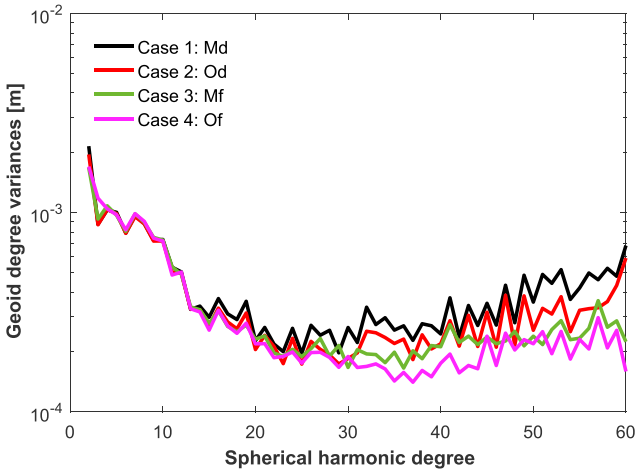


**Figure 3.** Gravity field solutions in terms of geoid degree variances w.r.t EIGEN6C4 determined by using the modified and optimized short-arc approaches (with and without modeling frequency-dependent noise).

As discussed in section 2.3, the optimized short-arc method is theoretically expected to improve the gravity field estimates compared to the modified short-arc approach. In order to discuss any possible practical merit of the optimized short-arc method in gravity field modeling, we compare four monthly gravity field models (indicated by cases 1 to 4) up to degree and order 60 derived from the GRACE observations over the month November 2014 via the modified and optimized short-arc approaches in the cases with and without modeling frequency-dependent noise. As given in Table 1, the variance-covariance matrices are diagonal matrices for cases 1 and 2 since the noise contained in the GRACE measurements are simply treated as white noise in the two cases, while they become full matrices when the frequency-dependent noise is modeled in accordance with section 3.1. During computing the four models, the arc length is chosen to be 2 hr since Chen et al. (2015) found that such an arc length can achieve the optimum gravity field model for the modified short-arc approach.

As expected, the derived gravity field solutions in terms of geoid degree variances relative to EIGEN6C4 (Förste et al., 2014) shown in Figure 3 demonstrate the clear improvements on gravity field determination

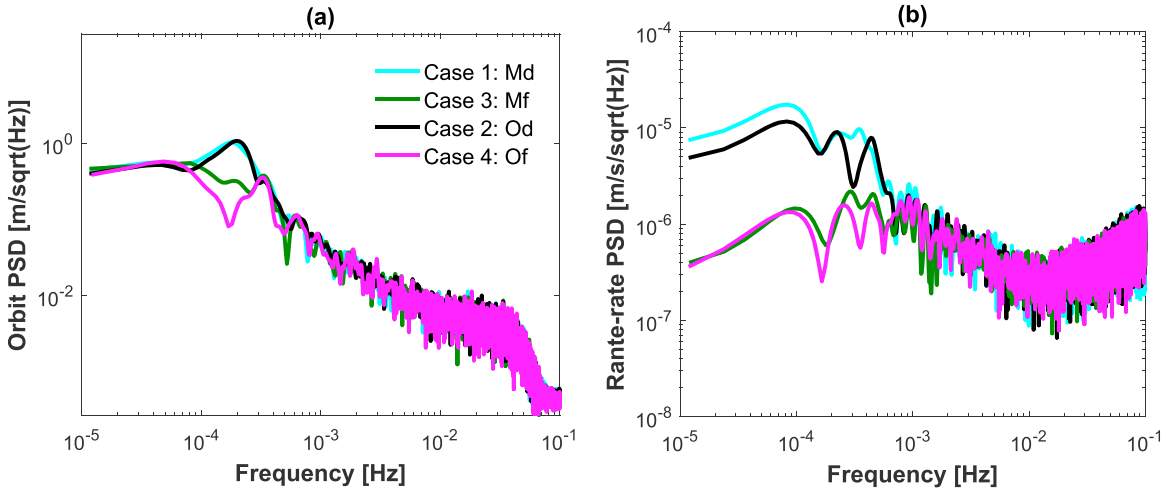


**Figure 4.** Power spectrum densities of postfit residuals of orbits (a) and range rate (b) measurements.

contributed by the optimized short-arc method. It can be concluded from Figure 3 that (1) no matter whether frequency-dependent noise is modeled or not, the optimized short-arc approach consistently reduces gravity field errors at high degrees significantly in comparison to the modified one and (2) the frequency-dependent noise modeling technique presented in this paper leads to prominent noise reductions for both modified and optimized short-arc methods. In mathematic sense, the optimized short-arc method is equivalent to the modified one. However, as elaborated in section 2.3, the optimized method is expected contribute a better-conditioned intermediate matrix in each arc, which is the reason for the improvements in cases 2 and 4. Detailed discussions on the difference of the property of the intermediate matrices between the two methods are going to be performed in section 3.3. In Figure 3, we also observe some differences at the low degrees ranging 2 to 3 between case 4 and others; nevertheless, such differences are less than 0.30 mm in terms of geoid degree variances. We further present the PSDs of the postfit residuals of observations (i.e., orbits and range rates) for the four cases in Figure 4 to check any possible enhancement caused by the optimized short-arc method in the observation domain. Overall, as indicated in Figure 4, the optimized short-arc method has stronger ability to reduce the low-frequency noise than the modified short-arc approach when comparing either case 1 to 2 or case 3 to 4. Particularly for the range rates, much more low-frequency noise is mitigated by the frequency-dependent noise modeling method, demonstrating the benefits of the proposed noise modeling.

In this study, the concurrent modeling of frequency-dependent noise for both orbit and range rate observations is one of the contributions. In order to separate the impact of frequency-dependent noise modeling on gravity field recovery from orbits to range rates, this study further calculates four GRACE solutions up to degree and order 60 for the month November 2014 based on the strategies outlined in Table 2. The resulting gravity field solutions are illustrated in Figure 5 in terms of geoid degree variances relative to EIGEN6C4. One can see from Figure 5 that constructing variance-covariance matrices for either orbits or range rates, there is no doubt, improves the accuracies of geopotential coefficients at high degrees. Even better, simultaneously modeling the frequency-dependent noise for orbits and range rates further reduces the noise at high degrees. This finding supports that it is beneficial to consider the frequency-dependent noise in the orbit measurements during gravity field modeling in addition to that in the range rate data. Even though the coefficients of the four models at low degrees are generally dominated by geophysical signals, some slight discrepancies occur at degrees 2 and 3. In the comparison among the four models in terms of geoid degree variance, the maximum difference for degrees 2 and 3 is about 0.70 and 0.28 mm, respectively. Such discrepancies are probably caused by the differences among the constructed variance-covariance matrices. Therefore, an in-

**Table 2**
*Computational Schemes Based on Optimized Short-Arc Method*

| Gravity filed solution | Variance-covariance matrix | |
|---|---|---|
| | Orbits | Range rates |
| Case A: Od & Rd | Diagonal | diagonal |
| Case B: Of & Rd | Full | diagonal |
| Case C: Od & Rf | Diagonal | full |
| Case D: Of & Rf | Full | full |

*Note*. O = orbits; R = range rates; d = diagonal matrices; f = full matrices.

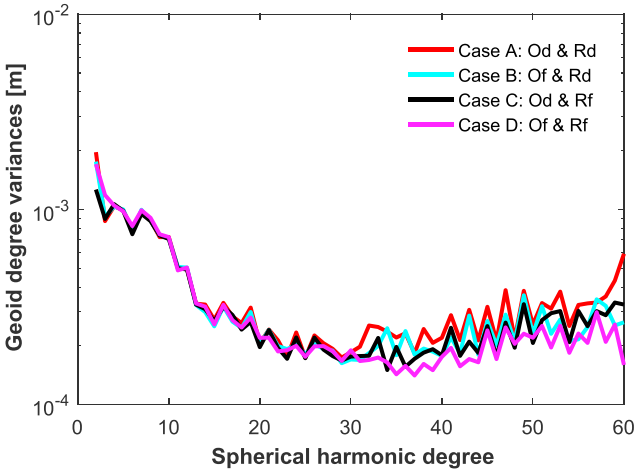


**Figure 5.** Gravity field solutions in terms of geoid degree variances w.r.t EIGEN6C4 determined by using the modified and optimized short-arc approaches with and without modeling frequency-dependent noise.

depth discussion on the impacts of different variance-covariance matrices on gravity field modeling deserves a separate investigation. Furthermore, we also plot the PSDs of the postfit residuals of orbits and range rates for cases A to D in Figure 6. It reveals that introducing variance-covariance matrices for any type of observables (orbit or range rate) achieves noise reductions for orbits and range rates at low frequencies, particularly for the range rates. Despite the relatively larger improvement contributed by modeling frequency-dependent noise in the range rate measurements, the decreased noise at low frequencies as shown in Figure 6a suggests that constructing variance-covariance matrix for orbits is beneficial as well.

### 3.3. Inversion Stability of the Modified and Optimized Short-Arc Methods

As stated in the introduction, one of the aims in this study is to answer whether we are able to prolong the arc length for the short-arc approach and what benefit this can achieve. The arc length used in the modified short-arc method is generally 2 hr (Chen et al., 2015). As discussed in section 2.3, further prolonging the arc length for the modified short-arc method is a challenge due to the unstable inversion of the large-scale intermediate matrix $\boldsymbol{D}_j\boldsymbol{Q}_j\boldsymbol{D}_j^T$, whose dimension is almost 7 times the arc length. In principle, the proposed optimized short-arc is able to extend the arc length since only two reduced-dimension matrices (namely, $\boldsymbol{D}_j^A$ and $\boldsymbol{D}_j^B$) are required to be inversed in forming the normal equation for estimating geopotential coefficients. To confirm the above this, we choose various arc lengths (2, 4, 6, 8, and 12 hr) and compute the corresponding condition numbers of $\boldsymbol{D}_j^s(s = A, B)$ based on the optimized short-arc approach. The same arcs are applied to the modified short-arc method and the condition numbers of $\boldsymbol{D}_j\boldsymbol{Q}_j\boldsymbol{D}_j^T$ are calculated as well. However, the case of 12 hr is unavailable for the modified short-arc method, since such a long arc length makes the dimension of the immediate matrix $\boldsymbol{D}_j\boldsymbol{Q}_j\boldsymbol{D}_j^T$ over 60,000, which requires almost 30 GB of computational memory. Considering the memory consumption of other matrices (e.g., the design matrices for generating normal equation and computing postfit residuals), the memory consumption in total is over 100 GB, which greatly exceeds the maximum memory (32 GB) of our computers. As shown in Table 3, the resulting condition number based on the modified short-arc method significantly increases with arc length, while it changes slightly when prolonging the arc length in the case of the optimized short-arc method. Even in the case of 2-hr arcs, the matrix $\boldsymbol{D}_j\boldsymbol{Q}_j\boldsymbol{D}_j^T$ generated via the modified short-arc method is still relatively ill

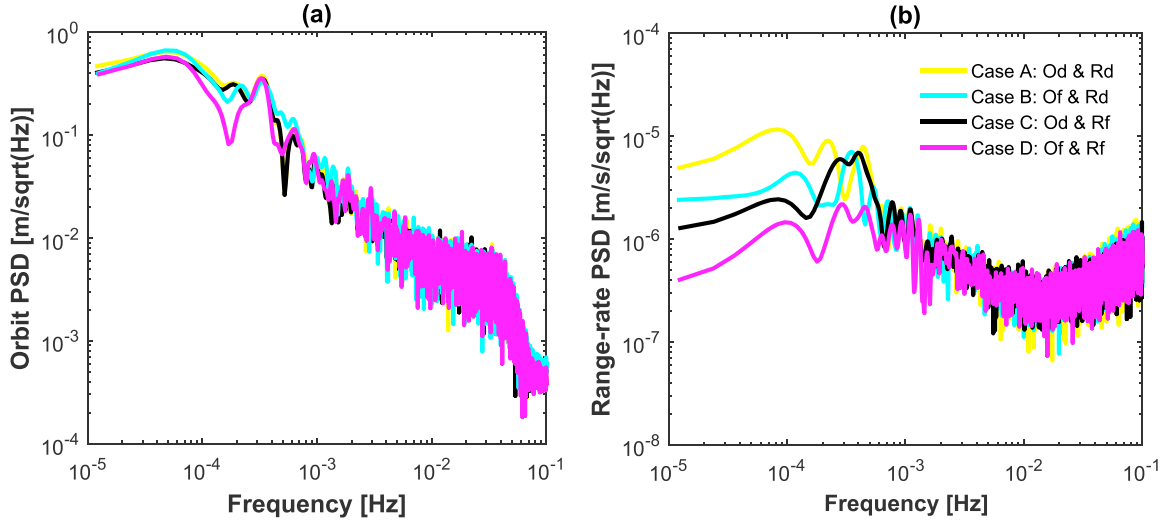


**Figure 6.** Power spectrum densities (PSDs) of postfit residuals of orbits (a) and range rate (b) measurements.

**Table 3**
*Condition Numbers of Intermediate Matrices Based on Various Arcs (Asterisk Indicates Unavailable Test)*

| | Modified short-arc method (log10) | Optimized short-arc method (log10) |
|---|---|---|
| Arc length (hr) | $\boldsymbol{D}_j\boldsymbol{Q}_j\boldsymbol{D}_j^T$ | $\boldsymbol{D}_j^s(s=A,B)$ |
| 2 | 15.3 | 3.3 |
| 4 | 15.8 | 4.2 |
| 6 | 16.4 | 4.8 |
| 8 | 16.8 | 5.5 |
| 12 | * | 9.9 |

conditioned, with the condition number of 15.3 (in unit of log10), which is remarkably larger than that generated by the optimized short-arc method.

In mathematic sense, the intermediate matrix $\boldsymbol{D}_j\boldsymbol{Q}_j\boldsymbol{D}_j^T$ applied to generate normal equation for estimating gravity field parameters in the modified short-arc approach is severely ill conditioned so that the property of the final normal matrix for solving gravity field parameters will be affected and eventually the gravity field estimates may be degraded. On the contrary, the condition number of the reduced-dimension intermediate matrix $\boldsymbol{D}_j^s(s=A,B)$ is significantly better, which will lead to more stable gravity field estimates. To verify it, the modified and optimized short-arc methods are separately applied to derive normal equations for estimating geopotential coefficients up to degree and order 60 from the GRACE data in November 2014, with different arc lengths listed in Table 3. The full variance-covariance matrices are built during deriving the above normal equations in accordance with section 3.1. As depicted in Table 4, the condition number of the final normal equation in terms of log10 for the modified short-arc method increases with the arc length. This agrees to what we discussed in section 2.3. In the case of the optimized one, the condition number shows an apparent decline when prolonging the arc length from 2 to 6 hr; however, it grows up when further prolonging the arc length from 6 to 12 hr. One possible reason for limiting the arc length, as shown in Table 3, is that the property of the immediate matrix $\boldsymbol{D}_j^s(s=A,B)$ degrades when the arc length is over 6 hr. Especially in the case of 12-hr arc length, $\boldsymbol{D}_j^s(s=A,B)$ becomes severely ill conditioned (with condition number of 9.9 in terms of log10). Nevertheless, the normal equation based on the optimized short-arc method has a smaller condition number than that based on the modified one when using the same arc length.

The more stable normal equations obtained by the optimized short-arc method are theoretically anticipated to improve gravity field estimation. To compare the difference of the practical contributions to gravity field estimation between the modified and optimized short-arc methods, we subsequently present the geoid degree variances of the corresponding gravity field models based on the above normal equations in Figure 7. One can see from Figure 7a that longer arcs (more than 2 hr) for the modified short-arc approach result in dramatic increase of noise in gravity field estimates as the normal equations become more ill conditioned. Conversely, as long as the arc length is no more than 6 hr, increasing arc length can lead to noticeable noise reduction in the obtained gravity field models for the case of the optimized short-arc method, which also agrees well with what we conclude from Table 4. However, for the case of the optimized short-arc approach, there is a slight noise growth in the estimated gravity field at high degrees when further prolonging the arc length from 6 to 12 hr. Overall, the most appropriate arc length is 2 hr for the modified short-arc method, while it is 6 hr for the optimized short-arc approach. Though 2-hr arcs are the optimal choice for the modified short-arc method, as demonstrated in Figure 8, the corresponding gravity field solution still manifests significant noise at high degrees compared to that determined by using the optimized short-arc method based on 6-hr arcs.

## 4. Development of Tongji-Grace2018 Monthly Solutions

**Table 4**
*Condition Numbers (log10) of Normal Matrices Based on Various Arcs (Asterisk Indicates Unavailable Test)*

| Arc length (hr) | Modified short-arc method | Optimized short-arc method |
|---|---|---|
| 2 | 6.24 | 6.12 |
| 4 | 6.43 | 5.90 |
| 6 | 6.57 | 4.82 |
| 8 | 6.76 | 5.84 |
| 12 | * | 5.90 |

The above analyses demonstrate the merits of the optimized short-arc approach in gravity field estimation. In view of such contributions of the proposed methodologies, we develop a new time series of GRACE monthly gravity field solutions (named Tongji-Grace2018) for the period April 2002 to August 2016 through using the optimized short-arc approach. Like the official RL06 models (i.e., CSR RL06, GFZ RL06, and JPL RL06), Tongji-Grace2018 is provided in two different maximum resolutions (d/o 96 and 60). This section is dedicated to elaborating the dynamic process models and observations collected by GRACE satellites as well as the detailed parameter estimation process for generating Tongji-Grace2018 models.

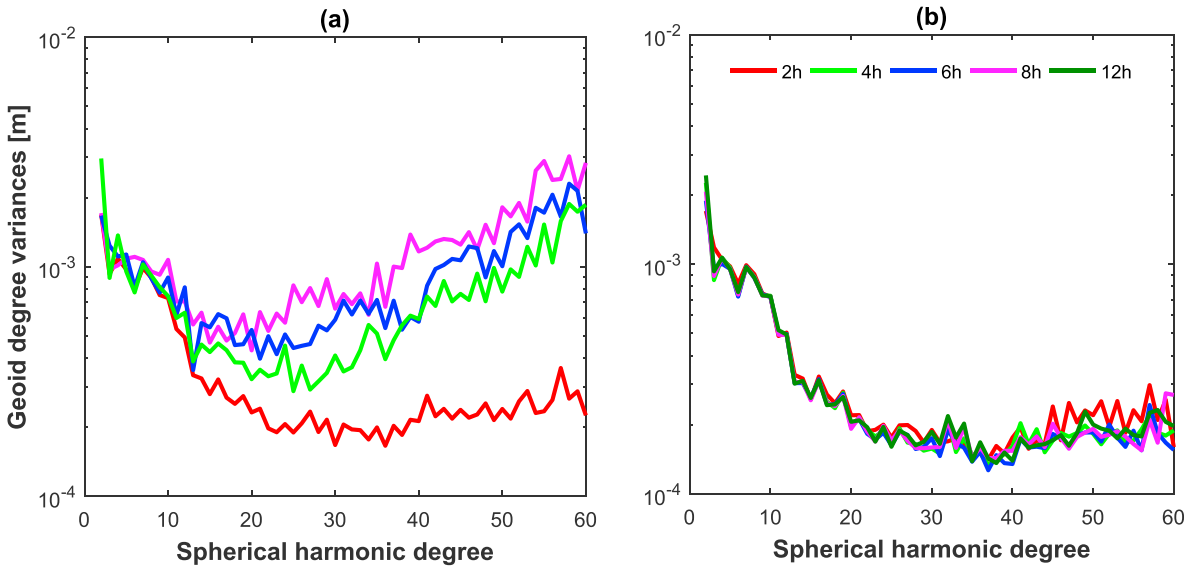


**Figure 7.** Gravity field solutions in terms of geoid degree variances w.r.t EIGEN6C4 determined by using the modified (a) and optimized (b) short-arc approaches on the basis of various arc lengths.

### 4.1. Models for Dynamic Process

Table 5 lists the dynamic models, including static Earth's gravity field, solid Earth (pole) tides, ocean (pole) tides, atmospheric and oceanic dealiasing effects, third-body perturbations, and relativistic impacts in conjunction with nongravitational forces. As we concentrate on the time-variable Earth's gravity field directly associated with the variations in atmosphere, ocean, ice sheet, hydrology, and solid Earth (Tapley et al., 2004), the dynamic forces should be accurately removed during gravity field modeling.

Since the GRACE monthly models are generally defined by a specific degree and order (e.g., 60, 96, or 120), high-degree signals are usually dealiased by static Earth's gravity field model. During deriving Tongji-Grace2018 models, the high-precision static GRACE-only Tongji-Grace02s complete to degree and order 180 is selected to account for the gravity field signals at high degrees. Like Chen et al. (2015), the impacts of the solid Earth (pole) tides in terms of geopotential coefficients for the degrees ranging 2 to 4 are modeled in accordance with the IERS 2010 conventions (Petit & Luzum, 2010). Unlike Chen et al. (2015) that only used 18 tides in EOT11a ocean model (Savcenko & Bosch, 2012), this paper considers two more ocean tide constituents (namely, Mtm and Msqm) from Fes2004 (Lyard et al., 2006) in addition to the 18 tides in EOT11a to remove the impacts of the ocean tides. As stated in Petit and Luzum (2010), the secondary ocean tides may represent almost 20% of impacts on satellite orbit integration based on one day arcs, thus an admittance method proposed by Rieser et al. (2012) is used to linearly interpolate 236 secondary ocean tides. For the purpose of computing the corrections due to the ocean pole tides, Desai model (Desai, 2002) up to degree and order 100 is adopted. For the removal of the short-period nontidal variability over the atmosphere and ocean, the AOD1B RL06 up to degree and order 180 is employed (Dobslaw et al., 2017). As for the relativistic effects, we calculate the corresponding correction in terms of acceleration based on the IERS 2010 conventions. For computing the third-body perturbations caused by the Sun, the Moon, and other planets (e.g., Jupiter), the version of planetary ephemerides offered by JPL, namely, DE430 (Folkner et al., 2008), is used to determine the precise position and velocity vectors for planets at any required epoch. Regarding calculation of the nongravitational forces acting on satellites, the onboard accelerometer data are employed.

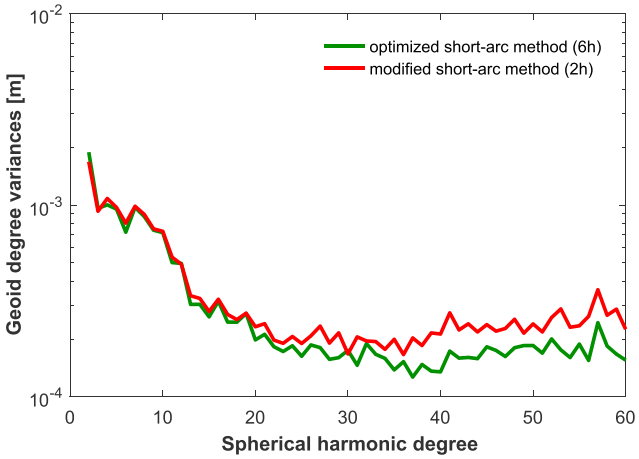


**Figure 8.** Gravity field solutions in terms of geoid degree variances w.r.t EIGEN6C4 determined by using the modified (2-hr arcs) and optimized (6-hr arcs) short-arc approaches.

**Table 5**
*Dynamic Models*

| Force model | Description |
|---|---|
| Static Earth's gravity field | Tongji-Grace02s with a maximum degree and order of 180 |
| Solid Earth tides | IERS 2010 conventions (Petit & Luzum, 2010) |
| Solid Earth pole tides | IERS mean pole |
| Ocean tides | EOT11a (Savcenko & Bosch, 2012) & Fes2004 (Mtm & Msqm; Lyard et al., 2006) up to d/or 100 |
| Ocean pole tides | Desai model (Desai, 2002) up to d/o 100 |
| Atmospheric and oceanic dealiasing | AOD1B RL06 dealiasing products (Dobslaw et al., 2017) up to d/o 180 |
| Third body | The Sun, the Moon, and Jupiter (JPL DE430 planetary ephemerides; Folkner et al., 2008) |
| Relativistic impacts | IERS 2010 conventions |
| Nongravitational forces | Onboard accelerometer data |

### 4.2. Satellite Observations

The creation of normal equation (22) for estimating gravity field parameters is based on GRACE observations containing orbits and accelerations as well as attitudes of both satellites together with intersatellite range rates, which are the primary observation type of GRACE Level-1b data published by JPL. As stated in the introduction, every release of GRACE Level-1b data can lead to apparent improvements on gravity field estimation, which is one of the reasons for JPL to recently reprocess the GRACE Level-1b data by using refined data processing algorithms, leading to an improved version of Level-1b data called GRACE RL03. This paper therefore uses the accelerations and attitudes of the twin satellites and the intersatellite range rates from GRACE RL03 as well as kinematic orbits from Graz University of Technology (Zehentner & Mayer-Gürr, 2013). The basic information on the employed measurements is given in Table 6.

### 4.3. Parameter Estimation

Based on the dynamic models given in Table 5 and the measurements outlined in Table 6, the subnormal equation (22) regarding the unknown vector $\boldsymbol{x}_j$ for each arc can be computed. The vector $\boldsymbol{x}_j$ to be estimated includes global (gravity field coefficients) and local (boundary positions and accelerometer scales and biases) parameters as elaborated in section 2.2. Because Meyer et al. (2016) showed that calibrating accelerometer data via daily scales can considerably mitigate the impacts of the solar activity on the derived gravity field models, we estimate daily accelerometer scales in three axes for both satellites throughout this study. To model any possible time-related variation in daily accelerometer biases, the accelerometer bias in each axis of the accelerometer is treated as a 5-order polynomial for each day in accordance with Chen et al. (2018). Although the local parameters (boundary parameters and accelerometer parameters) are simultaneously estimated with the geopotential coefficients, it is worth noting that the boundary parameters are eliminated from the subnormal equation for each arc and the accelerometer parameters are eliminated for each day. All the reduced daily normal equations are subsequently accumulated to form the monthly normal equation for solving the geopotential coefficients up to degree and order 96 (or 60). Even though all the local parameters are eliminated from the final normal equation, the corresponding gravity field result is mathematically equivalent to the case of retaining the local parameters in the final normal equation.

**Table 6**
*Measurement Information*

| Observable | Description |
|---|---|
| Orbit | Kinematic orbits from Graz University of Technology; sampling rate of 10 s |
| Range rate | Sampling rate of 5 s |
| Attitude | Sampling rate of 5 s |
| Acceleration | Sampling rate of 1 s; resampled into 5 s |

Chen et al. (2018) showed that accurately modeling the time-related variations in accelerometer parameters can lead to improvements on gravity field models. Here we present the statistics (mean values and standard deviations) of the estimated accelerometer scales and biases for the period April 2002 to August 2016 in Figure 9. It can be clearly observed in Figure 9 that both scales and biases experience apparent temporal variations, particularly in $X$ and $Z$ directions, indicating that the time-related variations in the accelerometer parameters should be accounted for during gravity field modeling.

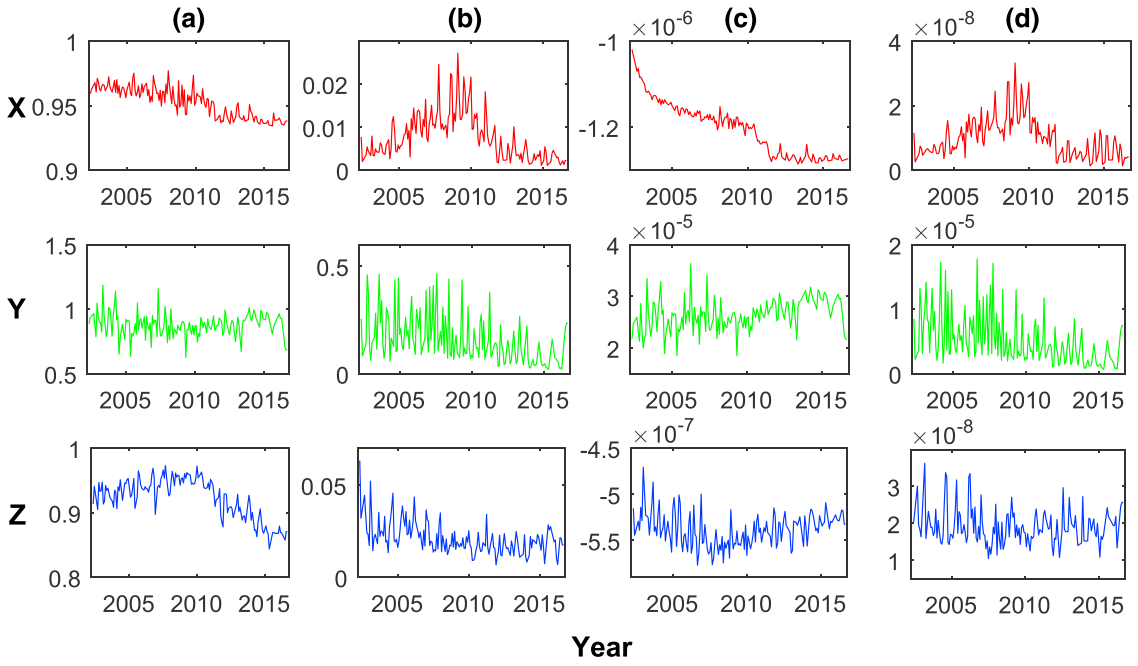


**Figure 9.** (a) Monthly mean accelerometer scales in *X*, *Y*, and *Z* axes. (b) Standard deviations of scales (in unit of meters per square second). (c) Monthly mean biases. (d) Standard deviations of biases (in unit of meters per square second).

## 5. Noise Analyses of Monthly Gravity Field Solutions

Since any gravity field model depends on specific observations, dynamic process models, and methodologies, either inaccuracies in the observations (or dynamic process models) or imperfectness in the methodologies will corrupt the derived gravity field model. Even though most of the GRACE monthly solutions available at International Centre for Global Earth Models (ICGEM) generally have comparable signal amplitudes, their noise levels are different. For gravity field modeling, the better methodology is able to considerably suppress the noise in addition to retaining the gravity field signals. As discussed in the preceding sections, the optimized short-arc method can reduce the gravity field noise at high degrees in comparison with the modified one. To comprehensively assess the quality of the Tongji-Grace2018 models derived on the basis of such optimized methodologies, the signal amplitude and noise level of the models are going to be discussed in terms of spectra, time, and space domains since each gravity field model simultaneously contains signals and noise.

### 5.1. Spectra Domain

To conduct analyses in the spectra domain for various GRACE models, the geoid degree variances with respect to the state-of-the-art static model EIGEN6C4 are computed. We compare Tongji-Grace2018 to CSR RL06, GFZ RL06, ITSG-Grace2018 (Mayer-Gürr et al., 2018), IGG RL01 (available at ICGEM), and HUST-Grace2016 (Zhou et al., 2017) for the months May 2003 and April 2011 in terms of geoid degree variances. Note that both IGG RL01 and HUST-Grace2016 are based on RL05 processing standards, but the others are all based on RL06 processing standards. It is well known that the GRACE-based geopotential coefficients at low degrees (particularly below degree 30) are generally dominated by gravity field signals, while the high-degree coefficients are contaminated by noise (Chen et al., 2018; Meyer et al., 2016). As presented in Figure 10, the signal levels (approximately below degree 30) of Tongji-Grace2018 for both months are in good agreement with those models on the basis of the RL06 processing standards. Compared to IGG RL01, HUST-Grace2016 and GFZ RL06, much more noise at degrees over 30 is reduced by Tongji-Grace2018 models. Even compared to CSR RL06, Tongji-Grace2018 still achieves clear noise reductions at degrees over 60, suggesting that our gravity field coefficients are accurate up to a higher degree. However, ITSG-Grace2018 has the best performance at high degrees, which is believed to be contributed by the rigorous variance-covariance matrices of observations constructed by incorporating the uncertainties of background force models (ocean model together with atmospheric and oceanic dealiasing product; Mayer-

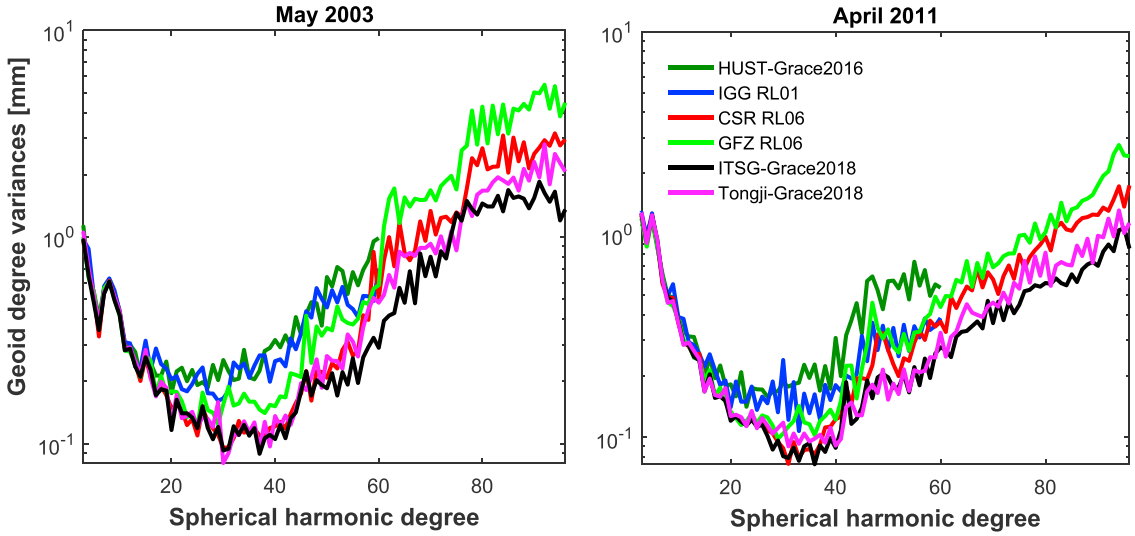


**Figure 10.** Geoid degree variances of various gravity field solutions.w.r.t EIGEN6C4.

Gürr et al., 2018). So far no data processing center except for Mayer-Gürr et al. (2018) has considered such uncertainties. One of the reasons for that is the tremendous computational burden caused by taking the background force models uncertainties into account.

The comparisons in terms of geoid degree variances only reflect the mean signal or noise per degree. To further compare the coefficients at all the degrees and orders among different GRACE models, we subsequently plot the discrepancies of geopotential coefficients between six GRACE models and EIGEN6C4 in Figure 11. In this case, the discrepancies at higher degrees and orders still are greatly contaminated by noise since the GRACE observations collected over one month are insensitive to high-degree signals. As shown in Figure 11, the zonal and near-zonal coefficients of both Tongji-Grace2018 and ITSG-Grace2018 in the case after degree 60 are better determined than those of other models. Especially compared to HUST-Grace2016 and IGG RL01, Tongji-Grace2018 and ITSG-Grace2018 show the significantly improved accuracies at high degrees.

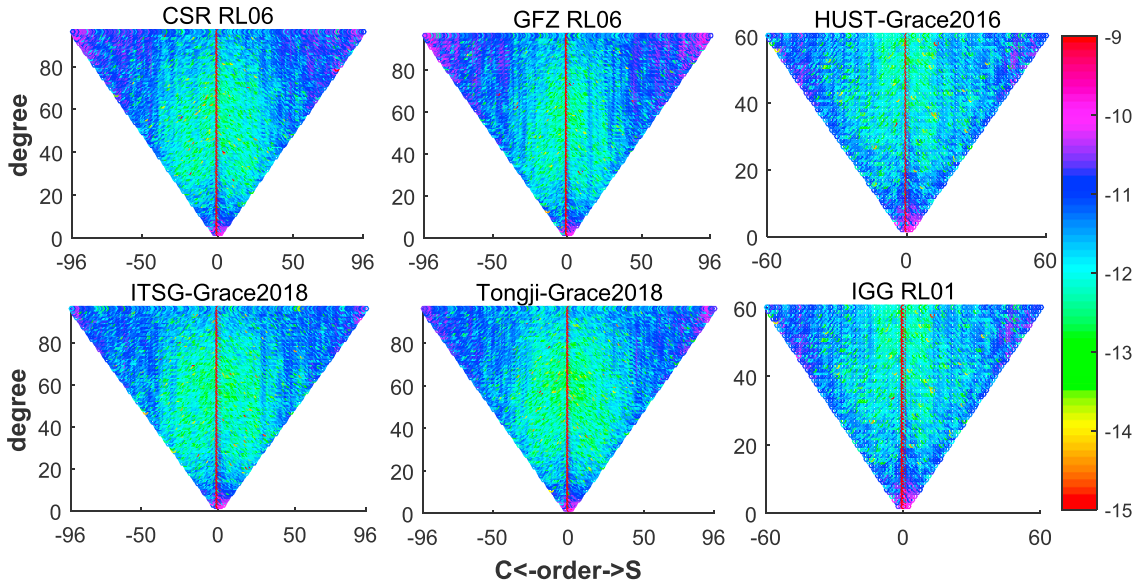


**Figure 11.** Geopotential coefficients differences (log10 scale) between six gravity field solutions and EIGEN6C4.

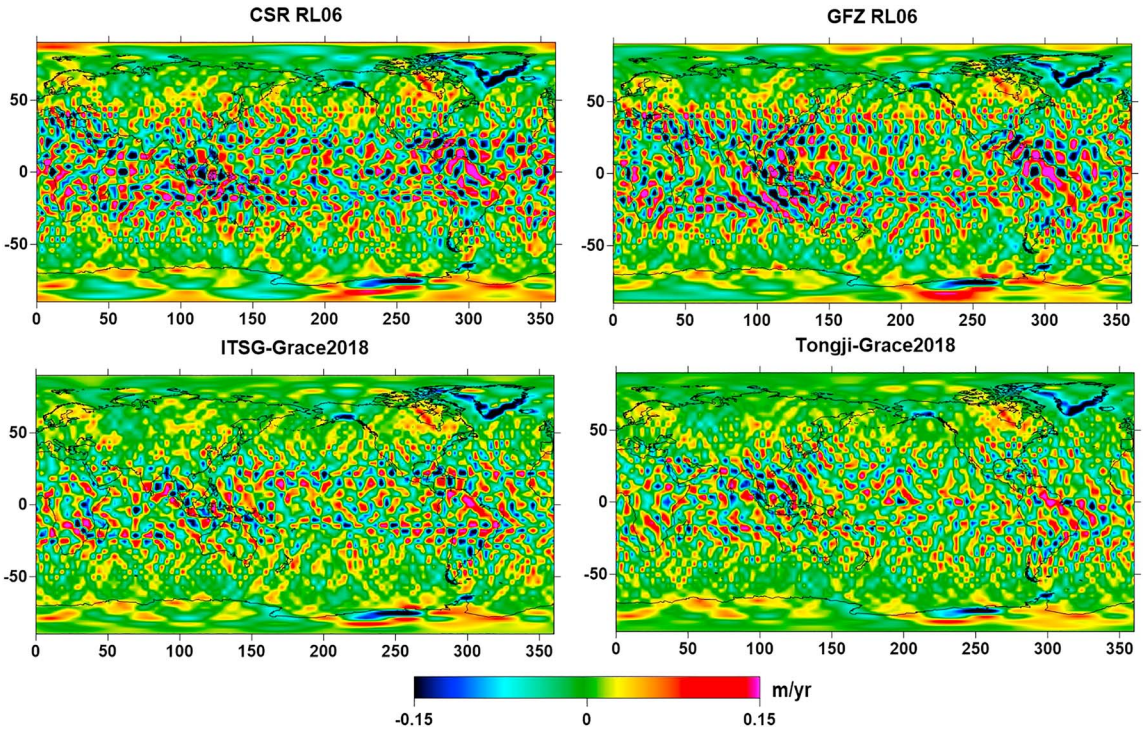


**Figure 12.** Global mass change trends derived from four GRACE models processed by $P_4M_6$ decorrelation filtering.

### 5.2. Spatial Noise

The improved accuracy in Tongji-Grace2018 is theoretically expected to enhance the estimates of global mass transports. Before the mass transports are computed, degree-1 coefficients are replaced with those from Swenson et al. (2008). For the $C_{20}$ coefficients, the SLR values determined by Cheng and Tapley (2004) are used instead of the GRACE-based ones. In this section, CSR RL06, GFZ RL06, and ITSG-Grace2018 are all complete to degree and order 96 and used for comparison. In an attempt to confirm possible improvement of Tongji-Grace2018 on the estimates of global mass transports, we estimate dominant signal terms (bias, trend, acceleration, annual, semiannual, and S2 alias components) after applying a $P_4M_6$ decorrelation filtering (Chen et al., 2009). The reason to apply the decorrelation filtering is that the GRACE models up to degree and order 96 are corrupted by so severe correlated noise that nearly no clear signal can be seen without using decorrelation filtering. Consequently, the global mass change trends (in $1^o \times 1^o$ grids) estimated from the four models are presented in Figure 12. It demonstrates that (1) striping noise over the zones near the equator are significantly suppressed in both Tongji-Grace2018 and ITSG-Grace2018 in comparison with those in CSR RL06 and GFZ RL06; (2) signal patterns over Greenland, Antarctica, North America, and South America derived from Tongji-Grace2018 and ITSG-Grace2018 are much clearer than those from other models; and (3) particularly in the polar areas, the signal patterns from Tongji-Grace2018 and ITSG-Grace2018 become significantly clearer in contrast with those from others.

Even though the decorrelation filtering has been applied to the four models, the corresponding mass change trends are still contaminated by the remaining noise. To considerably suppress the remaining noise, the Gaussian smoothing (Jekeli, 1981) with a reasonable smoothing radius will be employed in addition to the decorrelation filtering. It is worthwhile to point out that a larger smoothing radius will reduce the spatial resolution, but a smaller one may lead to much more remaining noise. Therefore, a reasonable smoothing radius should be consistent with the practical spatial resolution of the GRACE models. Considering the improvements of ITSG-Grace2018 and Tongji-Grace2018 with respect to others (CSR RL06 and GFZ RL06) at high degrees (particularly over 60) as shown in Figures 10 and 11, one may wonder whether the improved accuracies at high degrees allow for clear distinction of practical spatial resolution between the improved models (Tongji-Grace2018 and ITSG-Grace2018) and others. To answer this issue, a strategy is adopted as follows: The Gaussian smoothing with increasing smoothing radius (i.e., 100, 150, 200, 250,

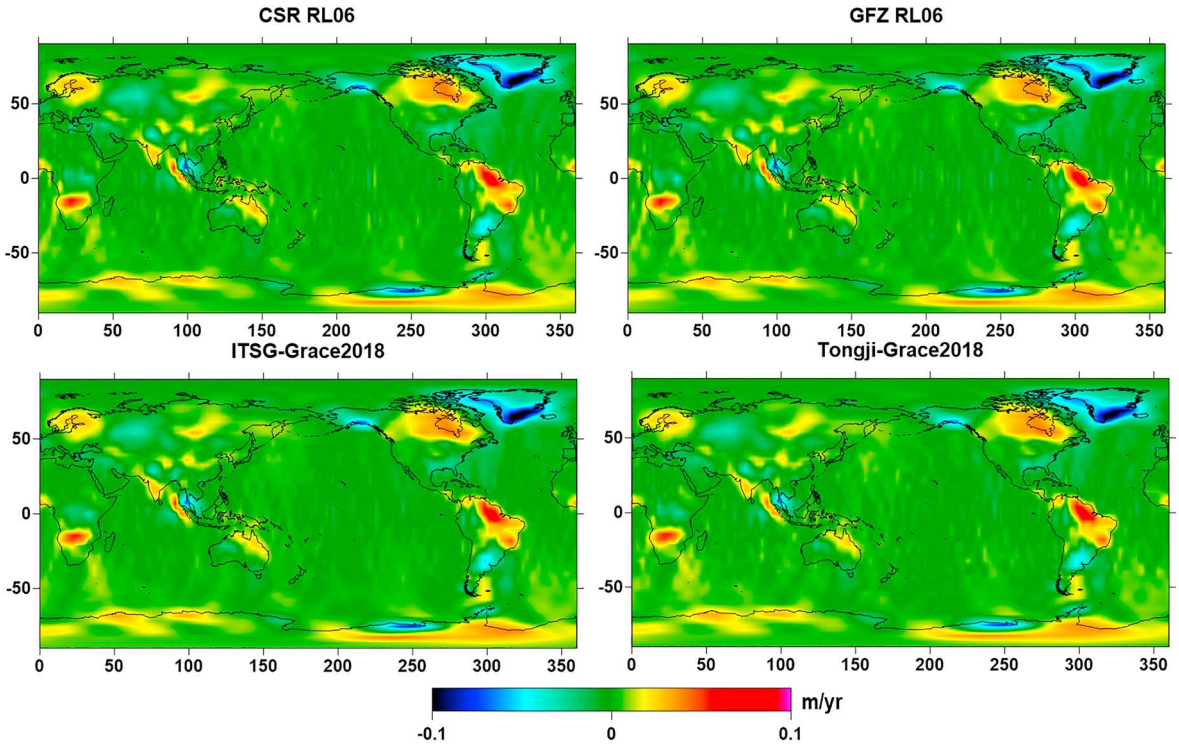


**Figure 13.** Global mass change trends estimated from four filtered GRACE models.

and 300 km) and the $P_4M_6$ decorrelation filtering are applied to process all the models up to the point that most striping noise in the global mass change trends estimated from either ITSG-Grace2018 or Tongji-Grace2018 disappear. As a consequence, the smoothing radius of 300 km is the point we are looking for, which reduces most striping noise in ITSG-Grace2018 and Tongji-Grace2018. Nevertheless, as presented in Figure 13, the corresponding global mass change trend maps from the four models over the period April 2002 to August 2016 do not show significant discrepancy in either signal pattern or striping noise. This finding indicates that the spatial resolutions of these GRACE models are overall comparable, which can be understandable since a lot of refined data processing strategies and up-to-date standards have been applied to improve all the models in terms of accuracies and resolutions (Bettadpur, 2018; Dahle et al., 2018; Mayer-Gürr et al., 2018; Yuan, 2018).

In physical sense, the spatial distributions of stripes to some extent are related to the GRACE orbit configuration. As explained in previous studies (e.g., Chen et al., 2018Dobslaw et al., 2016), the large orbit inclination (about 89°) for GRACE satellites leads to oversampling in the polar areas and sparser ground track coverage over medium and low latitude areas. As a consequence, much more striping errors over the medium- and low-latitude areas exist in all the models in contrast to over the polar areas. To further compare the noise distributions among the four models, RMS values of mass change residuals are depicted in Figure 14 for the period April 2002 to August 2016 after removing the estimated dominant signal terms (bias, trend, acceleration, annual, semiannual, and S2 alias). Since the dominant mass change signals have been subtracted and the oceanic tidal and nontidal effects have been modeled when solving the gravity field solutions (Chen et al., 2018), the resulting RMS values over ocean areas are approximately regarded as noise levels of the GRACE models in this study. One can see that the medium- and low-latitude areas are dominated by noise for the four models in spite of the significant noise reductions over the polar areas. As anticipated, much smaller RMS values over oceans are clearly observed in both Tongji-Grace2018 and ITSG-Grace2018 compared to in CSR RL06 and GFZ RL06.

Despite the significant noise reductions achieved by Tongji-Grace2018 and ITSG-Grace2018 in the case of only applying decorrelation filtering in comparison to CSR RL06 and GFZ RL06, the errors over oceans still cannot be completely neglected for any of the above models. Nevertheless, when the combined filtering (300-

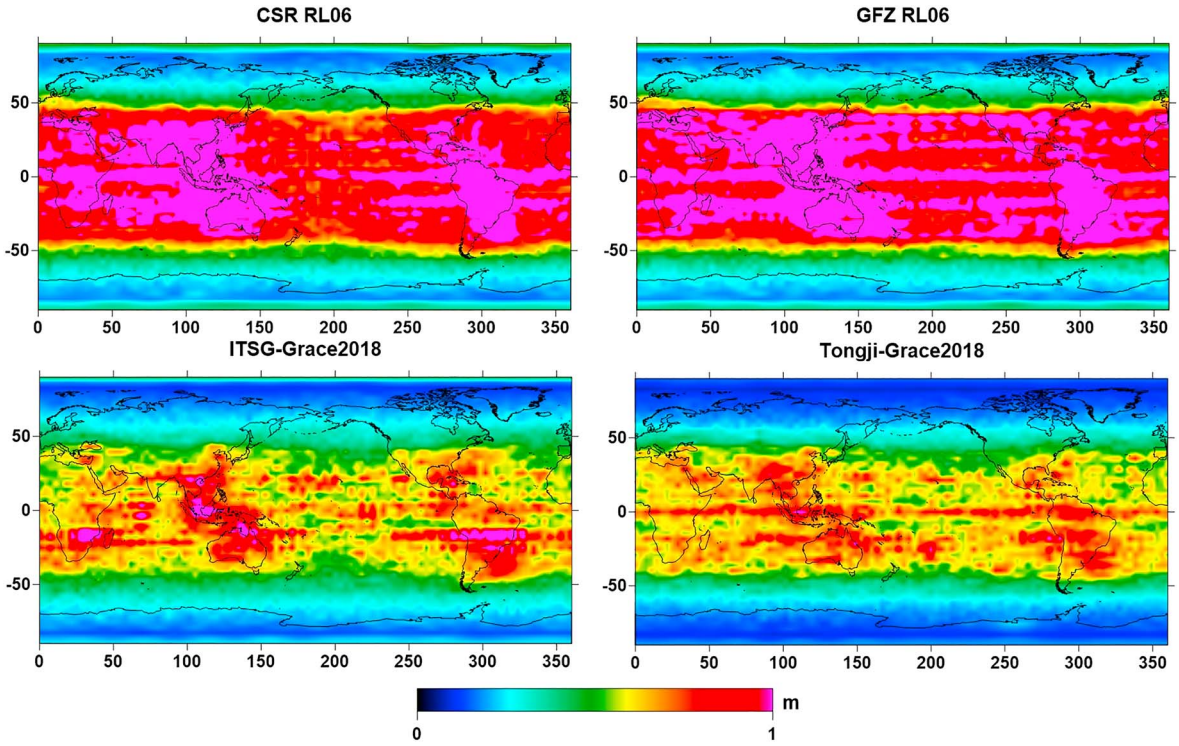


**Figure 14.** Root-mean-square values of global mass change residuals of GRACE models processed by decorrelation filtering.

km Gaussian smoothing and decorrelation filtering) are applied, the RMS values of residual mass changes are distinctly reduced for all the models, which are plotted in Figure 15. Even though the combined filtering effectively suppresses the noise in most areas, CSR RL06 and GFZ RL06 models still suffer from much more noise over ocean areas near the equator than both ITSG-Grace2018 and Tongji-Grace2018. The remaining mass variations over Greenland, Antarctica, North America, South America, Africa, and India are primarily caused by the signals not captured by the bias, trend, acceleration, annual, semiannual, and S2 alias parametrization. To quantify the noise levels of the four models, the mean RMS values over the global oceans in the decorrelation filtering and combined filtering cases are given in Table 7. One can see from Table 7 that Tongji-Grace2018 and ITSG-Grace2018 achieve much more noise decrease over oceans in both filtering cases when comparing to other models. For the case of Tongji-Grace2018, it reaches 35% and 7% of improvements with respect to CSR RL06 in the decorrelation filtering and combined filtering cases, respectively. It is a remarkable fact that the applied Gaussian smoothing contributes nearly 25 times noise reductions over oceans for CSR RL06 and GFZ RL06, but for Tongji-Grace2018, it only achieves about 17 times noise reductions. This finding suggests that the optimized methodologies applied to compute Tongji-Grace2018 greatly suppresses the spatial noise in gravity field estimates.

### 5.3. Temporal Noise Over Pacific and Sahara

The previous two subsections have discussed the noise behaviors of Tongji-Grace2018 models in the spectra and space domains. In this section, we primarily focus on noise comparisons among the above GRACE monthly solutions in the time domain. As motivated by the fact that the mass variations over oceans and deserts are anticipated to be smaller, this section studies the temporal noise behaviors of the above GRACE models over Pacific ($[28\text{N}, 51^{\circ}\text{N}],[170^{\circ}\text{E},220^{\circ}\text{E}]$) and Sahara desert ($[15^{\circ}\text{N},35^{\circ}\text{N}],[0^{\circ}\text{E},35^{\circ}\text{E}]$). Using the same analysis method as in section 5.2, the suitable Gaussian smoothing radius for the cases over Pacific and Sahara is determined to be 300 km as well. Based on the decorrelation filtering, the time series of mass changes over Pacific and Sahara in the time interval April 2002 to August 2016 from the four models are produced in the cases with and without using 300-km Gaussian smoothing. As depicted in Figure 16, clear discrepancies of mass changes between decorrelation filtering and combined filtering can be found.

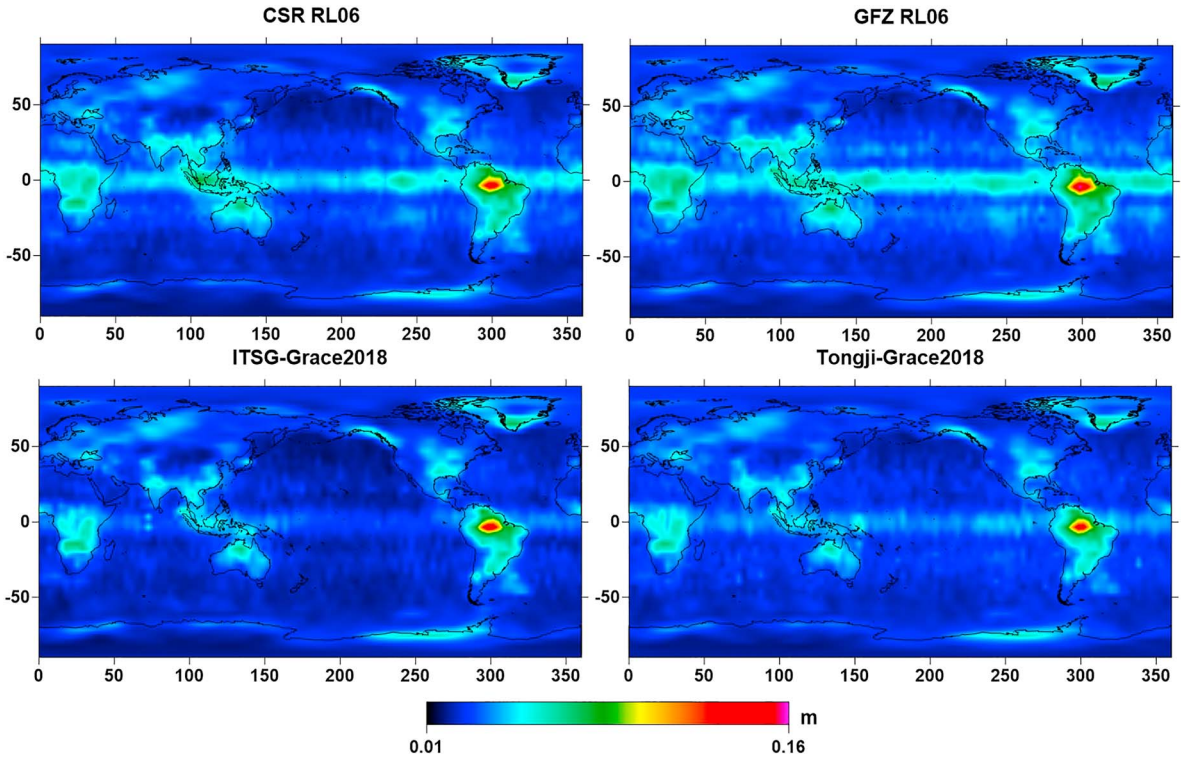


**Figure 15.** Root-mean-square values of the global mass change residuals of filtered GRACE models.

Over Pacific and Sahara, the mass changes on the basis of the four models show some differences in the case of only using decorrelation filtering.

To get more insights into the discrepancies among the four models, we further remove the primary signal terms (bias, trend, acceleration, annual, semiannual, and S2 alias terms) from the estimated mass changes and compute the RMS values of residuals. Following this method, the time series of RMS values together with the statistics for both decorrelation filtering and combined filtering cases are separately given in Figure 17 and Table 8 to describe the temporal variations in noise for different GRACE models over the two areas. Both Figure 17 and Table 8 demonstrate that Tongji-Grace2018 and ITSG-Grace2018 have less noise than other models. One can clearly see from Table 8 that, over Sahara desert, about 36% and 19% of noise is reduced by Tongji-Grace2018 relative to CSR RL06 in the decorrelation filtering and combined filtering cases, respectively. However, as indicated in Table 8, in the case of using the same decorrelation filtering, Tongji-Grace2018 and ITSG-Grace2018 based on 250-km Gaussian smoothing do not perform better than other two models based on 300-km Gaussian smoothing. In particular, for all the GRACE models, dramatic increases of noise occurred in early GRACE and some particular months (including September to October in 2004, June to July in 2012, and January to February in 2015). It is worth noting that the early GRACE suffered from missing observations (before 2003) and the above months experienced repeat ground track. However, the missing observations and repeat ground track directly impact the stability of normal equations, which eventually degrade the geopotential coefficients to be estimated. Especially for the high degrees (e.g., over degree 60), the impacts of missing observations and repeat ground track will become much more remarkable. In our own experiments (not shown), we truncated all the models to degree and order 60 and did the same noise analyses over Pacific and Sahara. As expected, the noise over those months with data quality degradation was found to be reduced to a great extent. We therefore believe the differences of noise levels among the four GRACE models over those months with poor observation condition as indicated in

**Table 7**
*Mean RMS Values (in Unit of Centimeters) of Mass Change Residuals Over the Global Oceans*

| Filtering | CSR RL06 | GFZ RL06 | ITSG-Grace2018 | Tongji-Grace2018 | Improvement rate |
|---|---|---|---|---|---|
| P4M6 | 68.6 | 72.0 | 48.0 | 44.7 | 35% |
| P4M6+Gauss | 2.8 | 2.9 | 2.4 | 2.6 | 7% |

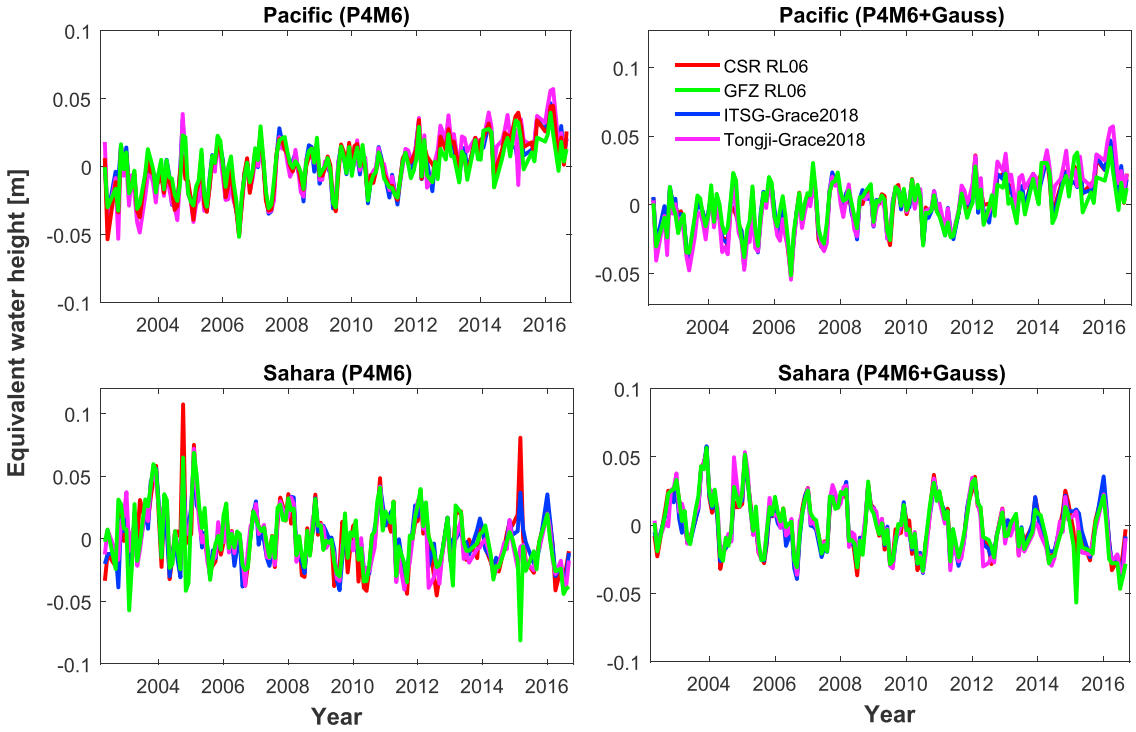


**Figure 16.** Time series of mass changes over Pacific and Sahara derived from GRACE models with and without Gaussian smoothing applied.

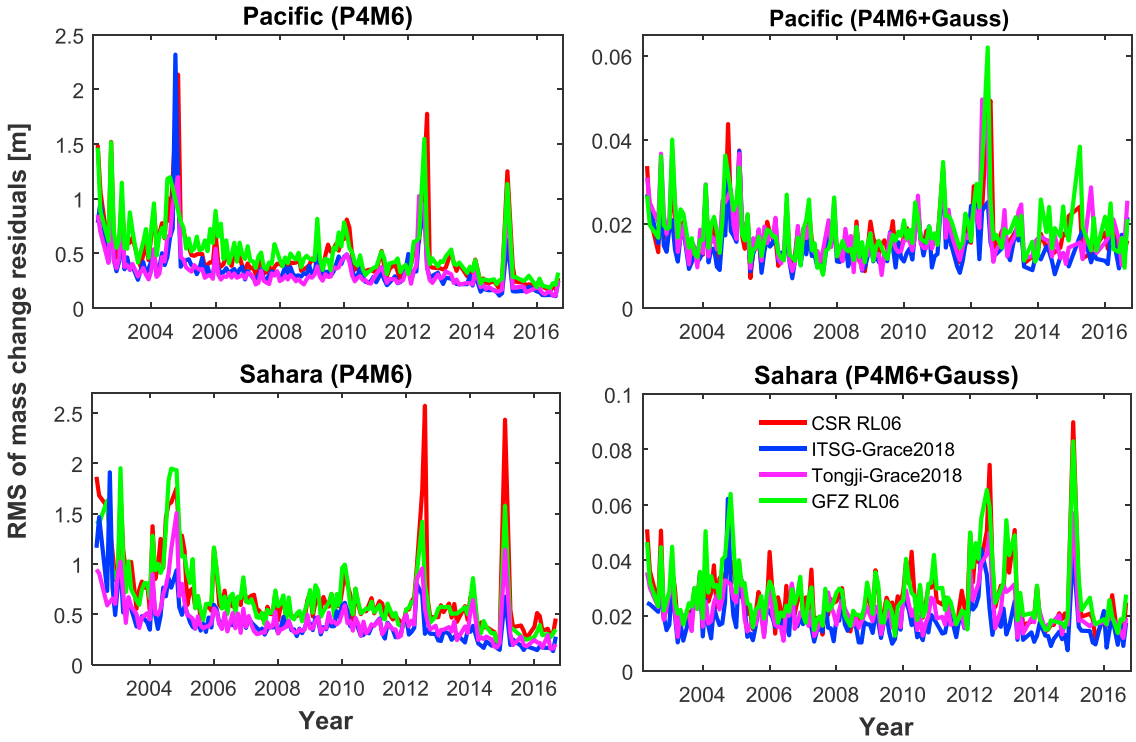


**Figure 17.** Time series of root-mean-square (RMS) values of residual mass changes derived from GRACE models.

**Table 8**
*Mean Root-Mean-Square Values (in Unit of Centimeters) of Mass Change Residuals Over Pacific and Sahara*

| Area | Filtering | CSR RL06 | GFZ RL06 | ITSG-Grace2018 | Tongji-Grace2018 | Improvement rate |
|---|---|---|---|---|---|---|
| Pacific | P4M6 | 53.6 | 59.2 | 36.4 | 38.2 | 29% |
| | P4M6+300km Gauss | 1.9 | 2.1 | 1.6 | 1.9 | 0% |
| | P4M6+250km Gauss | * | * | 2.3 | 2.8 | * |
| Sahara | P4M6 | 85.5 | 83.4 | 46.6 | 54.9 | 36% |
| | P4M6+300km Gauss | 3.1 | 3.3 | 1.9 | 2.5 | 19% |
| | P4M6+250km Gauss | * | * | 3.4 | 4.2 | * |

Figure 17 are mainly attributed to the differences of stabilities among varying gravity field modeling methods to the poor observation condition.

## 6. Signal Levels of Monthly Gravity Field Solutions

Every GRACE model simultaneously includes signals and noise. In view of the differences of the noise between Tongji-Grace2018 and other monthly gravity field models, further analyses on the signal levels of these models are conducted here. For comparisons of signal levels among the above models, this study selects four river basins and Greenland to see the mass changes related to hydrology process and ice melting, respectively.

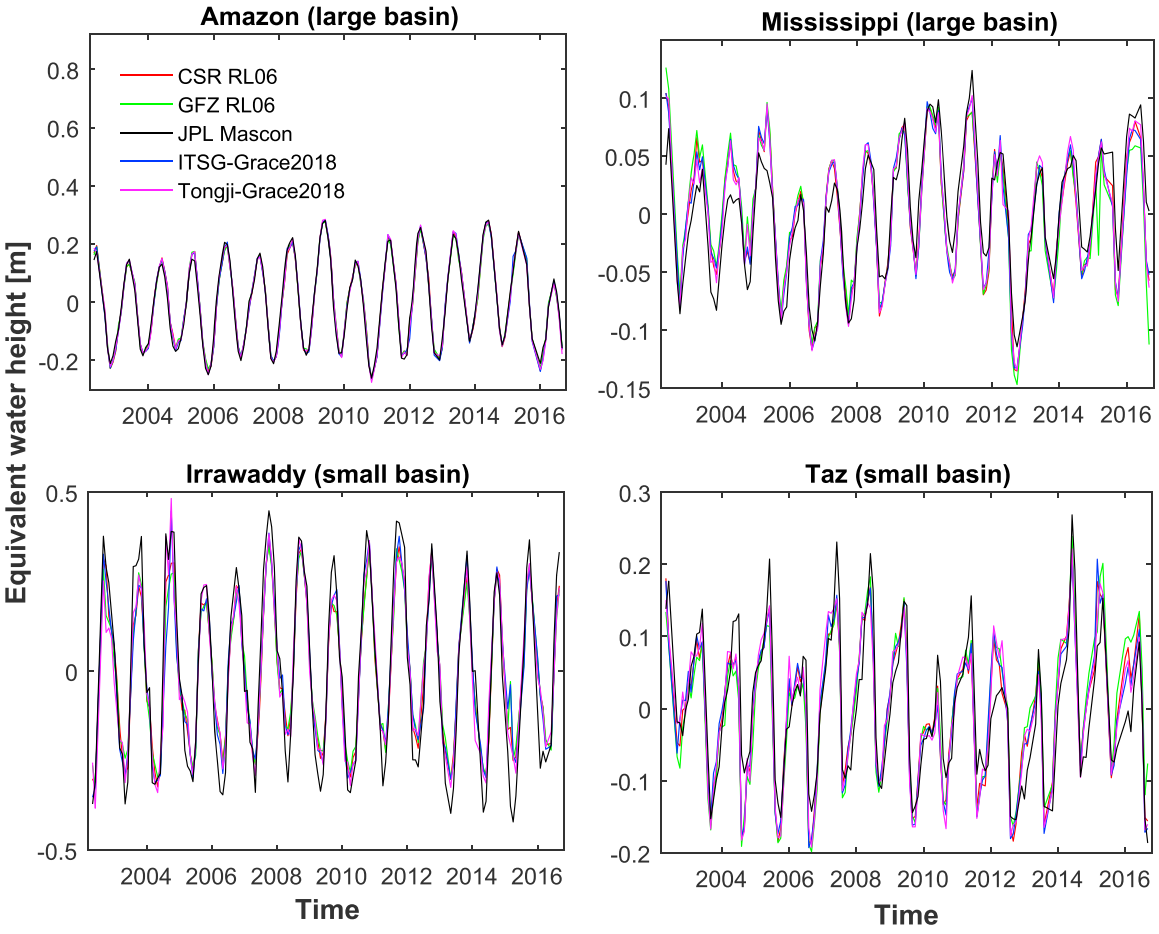


**Figure 18.** Time series of mass changes over river basins derived from mascon solution and filtered GRACE models.

**Table 9**
*Mean Annual Amplitudes and Phases Over River Basins*

| | CSR RL06 | GFZ RL06 | ITSG-Grace2018 | Tongji-Grace2018 | JPL Mascon |
|---|---|---|---|---|---|
| Area | Amplitude\| Phase | Amplitude\| Phase | Amplitude\|Phase | Amplitude\| Phase | Amplitude\| Phase |
| Amazon | ⟨22.8cm\| 96°⟩ | ⟨22.5cm\| 96°⟩ | ⟨23.4cm\| 98°⟩ | ⟨23.3cm\| 96°⟩ | ⟨24.7cm\| 111°⟩ |
| Mississippi | ⟨6.5cm\| 112°⟩ | ⟨6.4cm\| 111°⟩ | ⟨6.5cm\| 113°⟩ | ⟨6.6cm\| 111°⟩ | ⟨6.0cm\| 100°⟩ |
| Irrawaddy | ⟨26.6cm\| 291°⟩ | ⟨25.3cm\| 291°⟩ | ⟨27.3cm\| 290°⟩ | ⟨27.0cm\| 292°⟩ | ⟨34.8cm\| 296°⟩ |
| Taz | ⟨10.4cm\| 126°⟩ | ⟨10.6cm\| 126°⟩ | ⟨10.5cm\| 128°⟩ | ⟨10.7cm\| 128°⟩ | ⟨10.3cm\| 103°⟩ |

### 6.1. Time-Variable Signals Over River Basins

Considering that temporal behaviors of mass changes over river basins with different sizes may be varying, in this study, we select two large river basins (i.e., Amazon and Mississippi) and another two small river basins (i.e., Irrawaddy and Taz) to show the time-variable signals. The basic definitions of the four studied river basins are all taken from the Hydro website (http://hydro.iis.u-tokyo.ac.jp/~taikan/TRIPDATA/TRIPDATA.html). In this section, the following strategies are used in mass change estimates: (1) A $P_4M_6$ decorrelation filtering (Chen et al., 2009) in addition to Gaussian smoothing is applied during producing the time series of mass changes from the four GRACE models, and (2) to account for leakage issue, leakage biases are estimated by using least squares method and employed to correct GRACE-based mass changes (Klees et al., 2007). In view of the improved accuracies in Tongji-Grace2018 and ITSG-Grace2018, the Gaussian smoothing radius is chosen to be 250 km for them, while for the case of CSR RL06 and GFZ RL06, the corresponding smoothing radius is 300 km. The resulting time series of mass changes based on

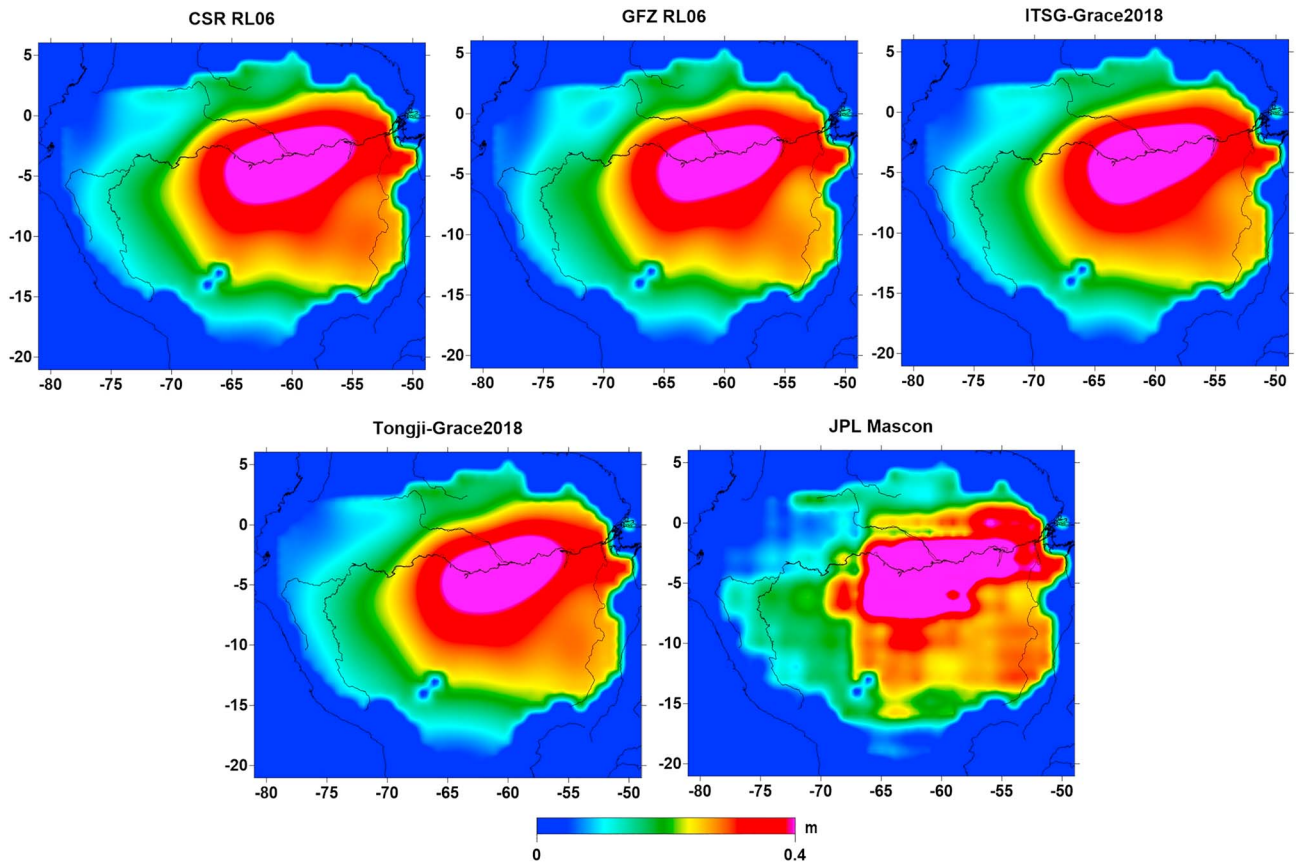


**Figure 19.** Annual amplitudes of mass changes over Amazon basin derived from different GRACE models.

**Table 10**
*Mean RMS and SNR values*

| | CSR RL06 | GFZ RL06 | ITSG-Grace2018 | Tongji-Grace2018 |
|---|---|---|---|---|
| Area | RMS\|SNR | RMS\|SNR | RMS\|SNR | RMS\|SNR |
| Amazon | ⟨281cm\| 0.08⟩ | ⟨407cm\| 0.06⟩ | ⟨213cm\| 0.12⟩ | ⟨263cm\| 0.09⟩ |
| Mississippi | ⟨232cm\| 0.03⟩ | ⟨393cm\| 0.02⟩ | ⟨158cm\| 0.04⟩ | ⟨195cm\| 0.04⟩ |
| Irrawaddy | ⟨245cm\| 0.11⟩ | ⟨328cm\| 0.08⟩ | ⟨174cm\| 0.16⟩ | ⟨216cm\| 0.12⟩ |
| Taz | ⟨94cm\| 0.12⟩ | ⟨144cm\| 0.08⟩ | ⟨80cm\| 0.14⟩ | ⟨68cm\| 0.17⟩ |

*Note*. RMS = root-mean-square; SNR = signal-to-noise ratio.

CSR RL06 and GFZ RL06, ITSG-Grace2018, and Tongji-Grace2018 are provided in Figure 18. Apart from the four time series of mass changes based on the filtered GRACE harmonic models, JPL RL06 Mascon solutions (Watkins et al., 2015) developed by using mascon technique are also included for comparison, since mascon technique is generally believed to improve the mass transport estimates (Luthcke et al., 2013; Save et al., 2016; Watkins et al., 2015). As we can see from Figure 18, Tongji-Grace2018 shows a good agreement with other models in terms of equivalent water heights over all the river basins. The correlation coefficients of

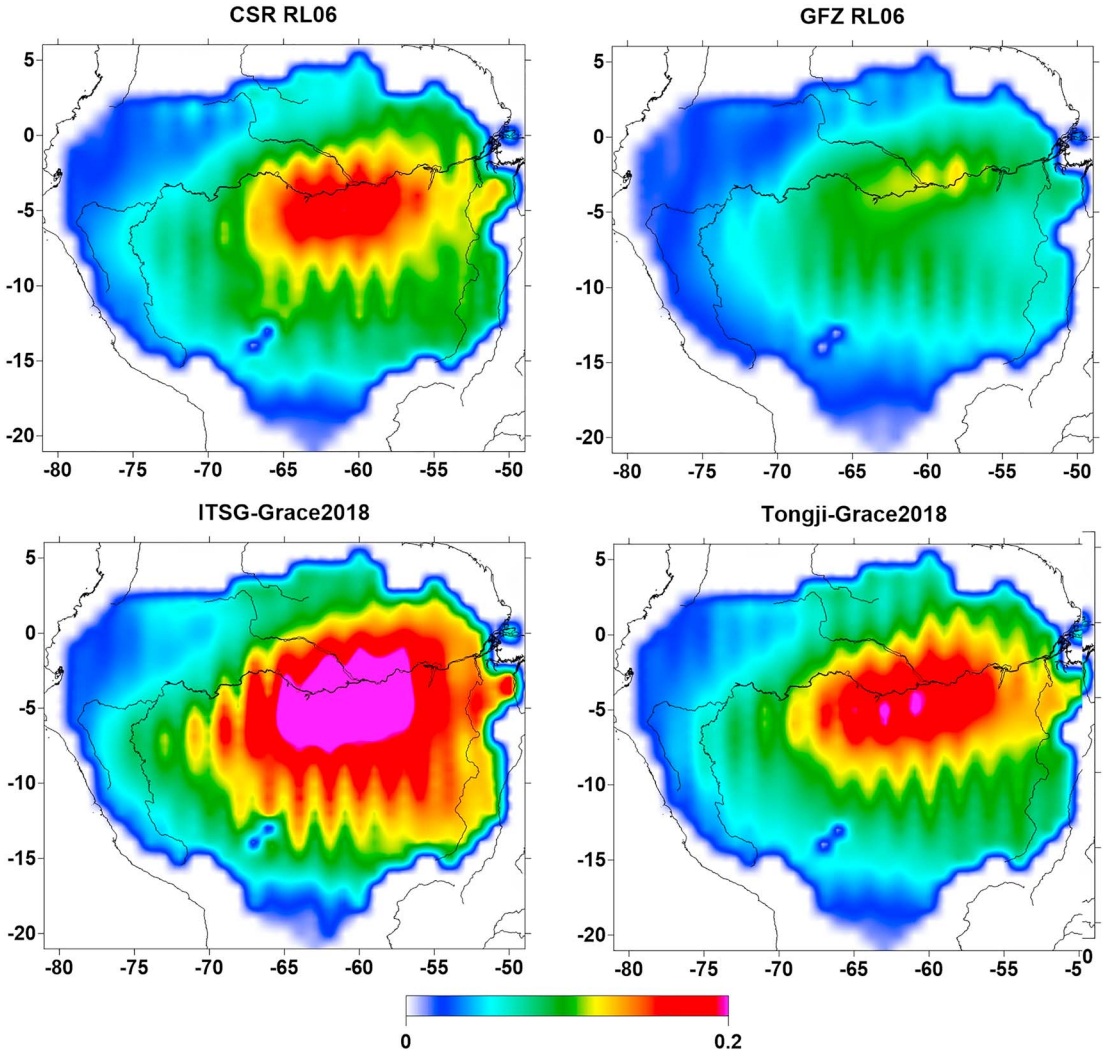


**Figure 20.** Signal-to-noise ratio values of mass changes over Amazon basin for different GRACE models.

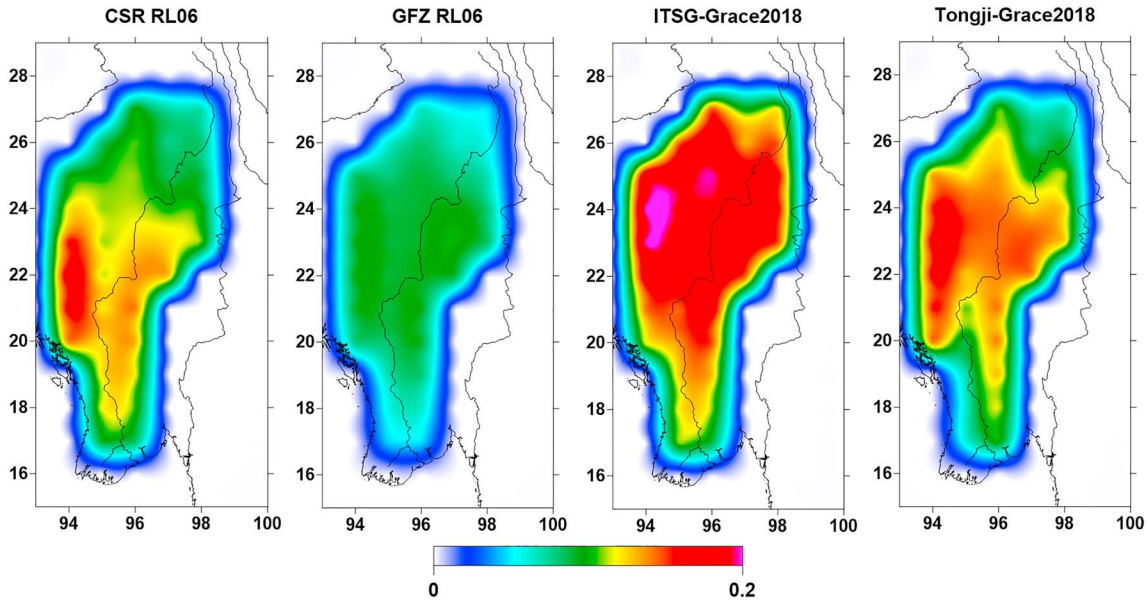


**Figure 21.** Signal-to-noise ratio values of mass changes over Irrawaddy basin for various GRACE models.

mass changes over the four regions between Tongji-Grace2018 and others are all over 92%. The comparable performances of Tongji-Grace2018 in both large and small river basins demonstrate that Tongji-Grace2018 is as sensitive as other models to hydrology signals though a smaller smoothing radius (250 km) is used. For quantifying the signal levels of the GRACE models, further analyses are carried out by estimating mean annual amplitudes and phases over the four river basins. As given in Table 9, the mean annual amplitudes and phases over the four basins estimated from Tongji-Grace2018 tend to be very close to those from other models (especially to CSR RL06, GFZ RL06, and ITSG-Grace2018). Both Figure 18 and Table 9 suggest that Tongji-Grace2018 and ITSG-Grace2018 are able to achieve the comparable mass changes as other solutions in the case of using a smaller smoothing radius (250 km).

For further comparison, we calculate the spatial distributions of annual amplitudes over Amazon basin estimated from the five models, which are displayed in Figure 19. Comparing the estimated annual amplitudes based on Tongji-Grace2018 to those derived from other models, a very good agreement can be found. Although the signal levels among different models are almost the same, the quality of various models is varying since every GRACE model contains both signals and noise. To reasonably assess the quality of the GRACE models except for mascon solution over the studied area, one feasible method is to separate the signals from noise and compute the SNR (signal-to-noise ratio) values. In order to do so, this analysis takes the following steps: (a) The primary signal terms (bias, trend, acceleration, annual, semiannual, and S2 alias components) are estimated from the postprocessed time series of mass changes (processed by filtering and corrected by leakage biases); (b) the residual mass changes are computed by subtracting the postprocessed mass changes from the unfiltered mass changes, and then the mean RMS values of residuals are approximately regarded as the noise of the unfiltered GRACE models since the residuals are severely contaminated by noise; (c) as the above four river basins are primarily contributed by annual signal, the estimated annual amplitudes can be regarded as signal; and (d) the computed annual amplitude along with the mean RMS values are eventually applied to derive the SNR values according to $SNR = Amplitude/RMS$. Note that we cannot do the same SNR analyses for JPL Mascon solution since the mascon solution has been postprocessed by using regularization technique and the noise of the unfiltered mascon solution is not accessible.

As a result, the mean RMS and average SNR values are presented in Table 10, which shows that the improvements contributed by Tongji-Grace2018 and ITSG-Grace2018 are significant. Among the four harmonic models, Tongji-Grace2018 and ITSG-Grace2018 have less noise and higher SNR over all the river basins. In comparison to CSR RL06, Tongji-Grace2018 has reduced the noise by 6% in Amazon, 22% in Mississippi, 12% in Irrawaddy, and 28% in Taz. In the four areas, the SNR values of Tongji-Grace2018 and

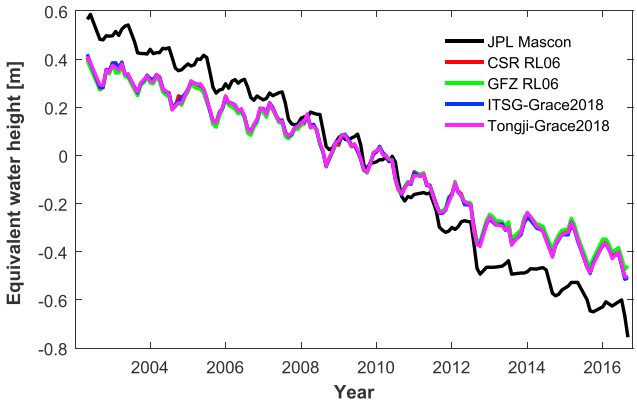


**Figure 22.** Time series of mass changes over Greenland derived from four GRACE models.

ITSG-Grace2018 are larger than those of CSR RL06 and GFZ RL06. Additionally, we plot the spatial distributions of the SNR values over the large river basin Amazon and small river basin Irrawaddy for the four harmonic models in Figures 20 and 21, separately. As shown in Figures 20 and 21, among the four harmonic models, Tongji-Grace2018 and ITSG-Grace2018 achieve the higher SNR values in both river basins. Even in the other two basins (results are not shown), the results are the same.

### 6.2. Mass Transport in Greenland

As one of the high-profile studied areas, Greenland is experiencing severe ice melting. The GRACE monthly solutions have been demonstrated to be sensitive to mass losses caused by the significant ice melting in Greenland (Velicogna, 2009). In an attempt to answer whether Tongji-Grace2018 models are able to retrieval mass losses related to ice melting, following the same postprocessing procedure as used in section 6.1, we compare the mass changes derived from Tongji-Grace2018 for the period April 2002 to August 2016 to those from other models (CSR RL06, GFZ RL06, ITSG-Grace2018, and JPL RL06 Mascon) in Figure 22. Here we should point out that the smoothing radius used for ITSG-Grace2018 and Tongji-Grace2018 is 250 km, while CSR RL06 and GFZ RL06 use a slightly larger smoothing radius of 300 km. Since the GIA impacts have been removed from JPL RL06 Mascon solution on the basis of ICE6G Glacial Isostatic Adjustment (GIA) model (Peltier et al., 2018), the same GIA model is applied to other GRACE models.

Interestingly, as indicated in Figure 22, the temporal behaviors of mass changes over Greenland among the four harmonic models are generally in good agreement, where the dramatic decrease of mass change and annual variation over Greenland can be captured by all the models. The correlation coefficients of mass changes between Tongji-Grace2018 and other three harmonic models are all more than 99.5%. However, compared to JPL Mascon solution, all the harmonic models suffer from apparent trend underestimates. Applying the same time series analysis method as used in section 6.1, the prominent signal components are estimated for the five models. The spatial distributions of the estimated trends from the five models are given in Figure 23. As we can observe from Figure 23, the four harmonic models agree well with each other, but JPL Mascon has much higher spatial resolution and stronger trend estimates. In Figure 23, most

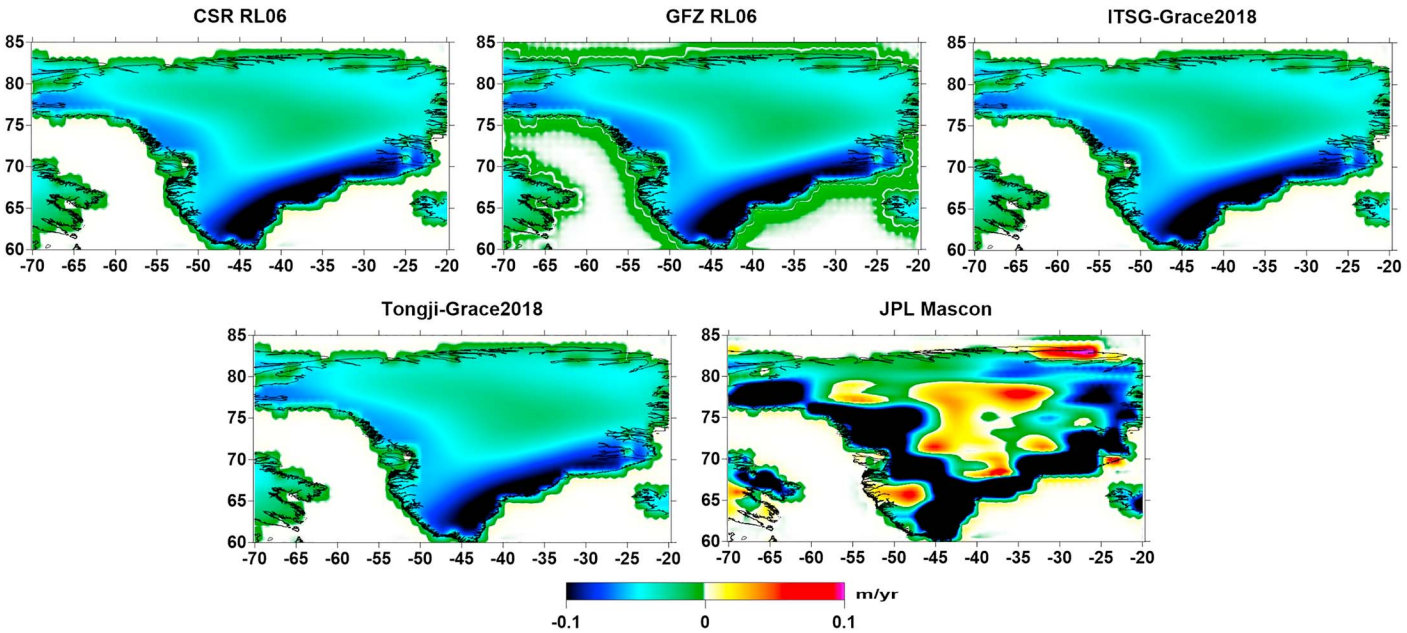


**Figure 23.** Trends of mass changes in Greenland derived from GRACE harmonic and mascon models.

**Table 11**
*Statistics of Mass Changes Over Greenland*

| Item | CSR RL06 | GFZ RL06 | ITSG-Grace2018 | Tongji-Grace2018 | JPL Mascon |
|---|---|---|---|---|---|
| Trend | −4.8 cm/year | −4.8 cm/year | −4.9 cm/year | −4.9 cm/year | −6.8 cm/year |
| Amplitude | 5.6 cm | 5.5 cm | 5.9 cm | 5.8 cm | 6.3 cm |
| Phase | 151° | 151° | 151° | 151° | 116° |
| RMS | 78cm | 98cm | 53cm | 46cm | * |

*Note*. JPL = Jet Propulsion Laboratory.

of the significant ice losses concentrate on West and South of Greenland. This study also presents the statistics of the mass changes over Greenland in Table 11. It reveals that the signal level of Tongji-Grace2018 is comparable to those of CSR RL06, GFZ RL06, and ITSG-Grace2018 in terms of trend, annual amplitude, and annual phase. Using the same noise analysis method as used in section 6.1, the mean RMS values of mass change residuals for the four harmonic models are also given in Table 11, which suggests that the least noise belongs to Tongji-Grace2018 over Greenland.

## 7. Conclusions

Although the GRACE mission came to an end in 2017, seeking for any improvement of current GRACE gravity field estimates is very important in both geodesy and geophysics. To improve the gravity field estimates, an optimized short-arc method is proposed to gravity field modeling in this paper. One drawback of the modified short-arc method presented in Chen et al. (2015) is that it needs the large-dimension intermediate matrix ($\boldsymbol{DQD^T}$) in equation (24) to be inversed prior to creating the normal equation. To overcome this drawback, the optimized method avoids direct inversion of ($\boldsymbol{DQD^T}$) through introducing an improved parameterization by treating boundary vectors in any integral arc as parameters to be solved. The improved parameterization makes matrix $\boldsymbol{D}$ an invertible matrix, which eventually allows the inversion of the intermediate matrix ($\boldsymbol{DQD^T}$) to be computed for orbits and range rate separately. In addition, with the purpose of accounting for the frequency-dependent noise in both kinematic orbits and range rates, the variance-covariance matrices for observations are constructed by using the noise whitening technique described in section 3.1. Numerical analyses of the optimized short-arc method demonstrate that (1) in comparison to the modified short-arc approach, the optimized short-arc approach greatly reduces the condition number of the final normal equation for estimating gravity field parameters, which eventually allows the arc length to be extended for the optimized method; (2) 6-hr arc length is demonstrated to be optimum for our improved approach since it achieves most significant noise reduction in gravity field estimation; (3) the constructed variance-covariance matrices for both orbits and range rates are beneficial for reducing the effects of frequency-dependent noise at low frequencies, which improves the derived gravity field solutions; (4) already for range rate observations, the benefits from modeling frequency-dependent noise are obvious, but concurrent frequency-dependent noise modeling for both orbit and range rate data can further decrease the noise in the estimated gravity fields; and (5) the optimized short-arc method consistently performs better than the modified short-arc approach, no matter whether frequency-dependent noise modeling is applied or not, since the inversion of the intermediate matrix $\boldsymbol{D}_j^s(s = A, B)$ in each integral arc has been stabilized.

Based on the optimized short-arc method, a refined time series of GRACE monthly solutions Tongji-Grace2018 is produced, which is available at the ICGEM (http://icgem.gfz-potsdam.de/ICGEM/). To investigate the quality of Tongji-Grace2018 models, we analyze the noise levels in terms of geoid degree variances and errors over oceans and desert together with signal levels over river basins and Greenland. Our analyses allow us to draw the following conclusions:

1. The geoid degree variance comparisons up to degree 96 among CSR RL06, GFZ RL06, HUST-Grace2016, IGG RL01, ITSG-Grace2018, and Tongji-Grace2018 suggest that the signal level of Tongji-Grace2018 at low degrees (below degree 30) is in a good agreement with others. Nevertheless, compared to CSR RL06 and GFZ RL06, the noise (above degree 60) in Tongji-Grace2018 in terms of cumulative geoid degree variance up to degree 96 is reduced by about 25% and 40%, respectively. Overall, Tongji-Grace2018 is closer to ITSG-Grace2018.

2. In the cases of applying decorrelation filtering and combined filtering, the global mass change trend estimated from Tongji-Grace2018 is less noisy than those from CSR RL06 and GFZ RL06. No matter whether Gaussian smoothing is employed or not, Tongji-Grace2018 reduces the noise over oceans in comparison with CSR RL06 and GFZ RL06; 35% and 7% of noise reductions over the global oceans relative to CSR RL06 are obtained by Tongji-Grace2018 in the cases of applying decorrelation filtering and combined filtering, respectively. Further investigations over Pacific and Sahara also confirm this result.
3. The comparable mass changes and amplitudes from Tongji-Grace2018 over river basins (Amazon, Mississippi, Irrawaddy, and Taz) and Greenland demonstrate that the signal amplitudes among the four models are comparable. The statistics results supports that the mass changes over the four river basins and Greenland from CSR RL06, GFZ RL06, ITSG-Grace2018, Tongji-Grace2018, and JPL Mascon are in good agreement, where the correlation coefficients are all over 92%. However, JPL Mascon solution overall has improved the mass transport estimates in terms of signal amplitude and spatial resolution. In spite of the comparable signal levels among the four harmonic models, the quality assessment results prove that Tongji-Grace2018 and ITSG-Grace2018 have less noise and higher SNR.

**Acknowledgments**
In our data processing, the GRACE Level-1b data (downloaded from ftp://podaac.jpl.nasa.gov) and Kinematic orbits (available at ftp://ftp.tugraz.at) are given by JPL and Graz University of Technology respectively. The GRACE monthly models for comparisons can be downloaded from ICGEM (http://icgem.gfz-potsdam.de/ICGEM/). Prof. Jürgen Kusche and Ms. Christina Lück from University of Bonn should be given our sincere acknowledgments for their help. This study is primarily sponsored by the National Natural Science Foundation of China (41731069), the National Key R&D Program of China (2017YFA0603103), and the Alexander von Humboldt Foundation in Germany, as well as partially supported by the National Natural Science Foundation of China (41674006). We are also very grateful to the editors, Prof. Paul Tregoning, and two anonymous reviewers' for their valuable comments, which significantly improve the quality of our original manuscript.

## References

Bettadpur S (2012). Gravity recovery and climate experiment UTCSR level-2 processing standards document for level-2 product release 0005, Center for Space Research, Uni. of Texas, Austin.

Bettadpur S (2018) UTCSR level-2 processing standards document for level-2 product release 0006. Technical Report GRACE, 327–742.

Broersen, P. M. (2000). Facts and fiction in spectral analysis. *IEEE Transactions on Instrumentation and Ieasurement*, *49*(4), 766–772. https://doi.org/10.1109/19.863921

Broersen, P. M., & Wensink, H. E. (1998). Autoregressive model order selection by a finite sample estimator for the Kullback-Leibler discrepancy. *IEEE Transactions on Signal Processing*, *46*(7), 2058–2061. https://doi.org/10.1109/78.700984

Chambers, D. P., & Bonin, J. A. (2012). Evaluation of Release-05 GRACE time-variable gravity coefficients over the ocean. *Ocean Science*, *8*(5), 859–868. https://doi.org/10.5194/os-8-859-2012

Chen, J. L., Li, J., Zhang, Z., & Ni, S. (2014). Long-term groundwater variations in Northwest India from satellite gravity measurements. *Global and Planetary Change*, *116*, 130–138. https://doi.org/10.1016/j.gloplacha.2014.02.007

Chen, J. L., Wilson, C. R., Blankenship, D., & Tapley, B. D. (2009). Accelerated Antarctic ice loss from satellite gravity measurements. *Nature Geoscience*, *2*(12), 859–862. https://doi.org/10.1038/ngeo694

Chen, Q., Shen, Y., Chen, W., Zhang, X., & Hsu, H. (2016). An improved GRACE monthly gravity field solution by modeling the non-conservative acceleration and attitude observation errors. *Journal of Geodesy*, *90*(6), 503–523. https://doi.org/10.1007/s00190-016-0889-6

Chen, Q., Shen, Y., Francis, O., Chen, W., Zhang, X., & Hsu, H. (2018). Tongji-Grace02s and Tongji-Grace02k: high-precision static GRACE-only global Earth's gravity field models derived by refined data processing strategies. *Journal of Geophysical Research: Solid Earth*, *123*(7), 6111–6137. https://doi.org/10.1029/2018JB015641

Chen, Q., Shen, Y., Zhang, X., Hsu, H., Chen, W., Ju, X., & Lou, L. (2015). Monthly gravity field models derived from GRACE level 1b data using a modified short arc approach. *Journal of Geophysical Research: Solid Earth*, *120*, 1804–1819. https://doi.org/10.1002/2014JB011470

Cheng, M. K., Shum, C. K., & Tapley, B. D. (1997). Determination of long-term changes in the Earth's gravity field from satellite laser ranging observations. *Journal of Geophysical Research*, *102*(B10), 22,377–22,390. https://doi.org/10.1029/97JB01740

Cheng, M. K., & Tapley, B. D. (2004). Variations in the Earth's oblateness during the past 28 years. *Journal of Geophysical Research*, *109*(B9), B09402. https://doi.org/10.1029/2004JB003028

Dahle C, Flechtner F, Gruber C, König D, König R, Michalak G, Neumayer KH (2012). GFZ GRACE level-2 processing standards document for level-2 product release 0005. Scientific Technical Report-Data, p.12, doi: 10.2312/GFZ.b103-1202-25.

Dahle, C., Flechtner, F., Gruber, C., König, D., König, R., Michalak, G., & Neumayer, K. H. (2014). GFZ RL05: An improved time-series of monthly GRACE gravity field solutions. In F. Flechtner, N. Sneeuw, & W.-D. Schuh (Eds.), *Observation of the system Earth from space—CHAMP, GRACE, GOCE and future missions*, (pp. 29–39). Berlin Heidelberg: Springer. https://doi.org/10.1007/978-3-642-32135-1_4

Dahle C, Murböck M, Michalak G, Neumayer KH, Flechtner F, Abrykosov O, et al.. The GFZ GRACE RL06 time series. EGU General Assembly 2018, May, 2018, Vienna.

Daras, I., & Pail, R. (2017). Treatment of temporal aliasing effects in the context of next generation satellite gravimetry missions. *Journal of Geophysical Research: Solid Earth*, *122*, 7343–7362. https://doi.org/10.1002/2017JB014250

Desai, S. D. (2002). Observing the pole tide with satellite altimetry. *Journal of Geophysical Research*, *107*(C11), 3186. https://doi.org/10.1029/2001JC001224

Ditmar, P., da Encarnação, J. T., & Farahani, H. H. (2012). Understanding data noise in gravity field recovery on the basis of intersatellite ranging measurements acquired by the satellite gravimetry mission GRACE. *Journal of Geodesy*, *86*(6), 441–465. https://doi.org/10.1007/s00190-011-0531-6

Ditmar, P., & van der Sluijs, A. A. E. (2004). A technique for Earth's gravity field modeling on the basis of satellite accelerations. *Journal of Geodesy*, *120*(3), 1804–1819.

Dobslaw, H., Bergmann-Wolf, I., Dill, R., Poropat, L., Thomas, M., Dahle, C., et al. (2017). A new high-resolution model of non-tidal atmosphere and ocean mass variability for de-aliasing of satellite gravity observations: AOD1B RL06. *Geophysical Journal International*, *211*(1), 63–269.

Dobslaw, H., Bergmann-Wolf, I., Forootan, E., Dahle, C., Mayer-Gürr, T., Kusche, J., & Flechtner, F. (2016). Modeling of present-day atmosphere and ocean non-tidal de-aliasing errors for future gravity mission simulations. *Journal of Geodesy*, *90*(5), 423–436. https://doi.org/10.1007/s00190-015-0884-3

Farahani, H. H., Ditmar, P., Inácio, P., Didova, O., Gunter, B., Klees, R., et al. (2017). A high resolution model of linear trend in mass variations from DMT-2: Added value of accounting for coloured noise in GRACE data. *Journal of Geodynamics*, *103*, 12–25. https://doi.org/10.1016/j.jog.2016.10.005

Farahani, H. H., Ditmar, P., Klees, R., Liu, X., Zhao, Q., & Guo, J. (2013). The static gravity field model DGM-1S from GRACE and GOCE data: Computation, validation and an analysis of GOCE mission's added value. *Journal of Geodesy*, *87*(9), 843–867. https://doi.org/10.1007/s00190-013-0650-3

Flechtner F and Dobslaw H (2013). AOD1B product description document for product release 05. GFZ German Research Centre for Geosciences.

Folkner WM, Williams JG, Boggs DH (2008). The planetary and lunar ephemeris DE 421. JPL IOM 343R-08-003.

Förste C, Bruinsma S, Abrikosov O, Flechtner F, Marty JC, Lemoine JM, et al. EIGEN-6C4—The latest combined global gravity field model including GOCE data up to degree and order 1949 of GFZ Potsdam and GRGS Toulouse. EGU General Assembly 2014, May, 2014, Vienna.

Guo, X., & Zhao, Q. (2018). GRACE time-varying gravity field solutions based on PANDA software. *Geodesy and Geodynamics*, *9*(2), 162–168. https://doi.org/10.1016/j.geog.2017.11.003

Guo, X., Zhao, Q., Ditmar, P., Sun, Y., & Liu, J. (2018). Improvements in the monthly gravity field solutions through modeling the colored noise in the GRACE data. *Journal of Geophysical Research: Solid Earth*, *123*, 7040–7054. https://doi.org/10.1029/2018JB015601

Jekeli C (1981). Alternative methods to smooth the Earth's gravity field. Report 327. Department of Geodetic Science and Surveying, Ohio State University, Columbus.

Klees, R., & Ditmar, P. (2004). How to handle colored noise in large least-squares problems in the presence of data gaps? In *V Hotine-Marussi Symposium on Mathematical Geodesy*, (pp. 39–48). Berlin, Heidelberg: Springer. https://doi.org/10.1007/978-3-662-10735-5_6

Klees, R., Zapreeva, E. A., Winsemius, H. C., & Savenije, H. H. G. (2007). The bias in GRACE estimates of continental water storage variations. *Hydrology and Earth System Sciences Discussions*, *11*(4), 1227–1241. https://doi.org/10.5194/hess-11-1227-2007

Koch, K. R., Kuhlmann, H., & Schuh, W. D. (2010). Approximating covariance matrices estimated in multivariate models by estimated auto-and cross-covariances. *Journal of Geodesy*, *84*(6), 383–397. https://doi.org/10.1007/s00190-010-0375-5

Kurtenbach, E., Mayer Gürr, T., & Eicker, A. (2009). Deriving daily snapshots of the Earth's gravity field from GRACE l1b data using Kalman filtering. *Geophysical Research Letters*, *36*, L17102. https://doi.org/10.1029/2009GL039564

Kusche, J., Klemann, V., & Bosch, W. (2012). Mass distribution and mass transport in the Earth system. *Journal of Geodynamics*, *35*(6), 1243–1249. https://doi.org/10.1007/s10712-014-9308-9

Lemoine J, Bourgogne S, Biancale R, Gégout P. The new GRGS-RL04 series of mass variations modeled with GRACE data. EGU General Assembly 2018, May, 2018, Vienna.

Liu, X., Ditmar, P., Siemes, C., Slobbe, D. C., Revtova, E., Klees, R., et al. (2010). DEOS mass transport model (DMT-1) based on GRACE satellite data: Methodology and validation. *Geophysical Journal International*, *181*(2), 769–788. https://doi.org/10.1111/j.1365-246X.2010.04533.x

Loomis, B. D., Nerem, R. S., & Luthcke, S. B. (2012). Simulation study of a follow-on gravity mission to GRACE. *Journal of Geodesy*, *86*(5), 319–335. https://doi.org/10.1007/s00190-011-0521-8

Luthcke, S. B., Sabaka, T. J., Loomis, B. D., Arendt, A. A., McCarthy, J. J., & Camp, J. (2013). Antarctica, Greenland and Gulf of Alaska land-ice evolution from an iterated GRACE global mascon solution. *Journal of Glaciology*, *59*(216), 613–631. https://doi.org/10.3189/2013JoG12J147

Lyard, F., Lefevre, F., Letellier, T., & Francis, O. (2006). Modelling the global ocean tides: Modern insights from FES2004. *Ocean Dynamics*, *56*(5-6), 394–415. https://doi.org/10.1007/s10236-006-0086-x

Mayer-Gürr T (2006). Gravitationsfeldbestimmung aus der Analyse kurzer Bahnbögen am Beispiel der Satellitenmissionen CHAMP und GRACE, Dissertation, University of Bonn.

Mayer-Gürr, T, Behzadpour S, Ellmer M, Klinger B, Kvas, A, Strasser S, Zehentner N (2018). ITSG-Grace2018: The new GRACE time series from TU Graz. Abstract from GRACE/GRACE-FO Science Team Meeting 2018, Oct, 2018, Potsdam, Germany.

Mayer-Gürr, T., Savcenko, R., Bosch, W., Daras, I., Flechtner, F., & Dahle, C. (2012). Ocean tides from satellite altimetry and GRACE. *Journal of Geodynamics*, *59-60*, 28–38. https://doi.org/10.1016/j.jog.2011.10.009

Mayer-Gürr T, Zehentner N, Klinger B, Kvas A. ITSG-Grace2014: A new GRACE gravity field release computed in Graz. Oral presentation at the GRACE Science Team Meeting, September, 2014, Potsdam.

Meyer, U., Jäggi, A., Jean, Y., & Beutler, G. (2016). AIUB-RL02: An improved time-series of monthly gravity fields from GRACE data. *Geophysical Journal International*, *205*(2), 1196–1207. https://doi.org/10.1093/gji/ggw081

Peltier, W. R., Argus, D. F., & Drummond, R. (2018). Comment on "An assessment of the ICE-6G_C (VM5a) glacial isostatic adjustment model" by Purcell et al. *Journal of Geophysical Research: Solid Earth*, *123*(2), 2019–2028. https://doi.org/10.1002/2016JB013844

Petit G and Luzum B (2010). IERS conventions (2010) (No. IERS-TN-36), Bureau International Des Poids et Mesures Sevres, France.

Rieser D, Mayer-Gürr T, Savcenko R, Bosch W, Wünsch J, Dahle C, Flechtner F (2012). The ocean tide model EOT11a in spherical harmonics representation.

Savcenko R and Bosch W (2012). EOT11a—Empirical ocean tide model from multi-mission satellite altimetry. DGFI Report No. 89.

Save, H., Bettadpur, S., & Tapley, B. D. (2016). High-resolution CSR GRACE RL05 mascons. *Journal of Geophysical Research: Solid Earth*, *121*, 7547–7569. https://doi.org/10.1002/2016JB013007

Schneider M (1968). A general method of orbit determination. Report 1279, Royal Aircraft Establishment, Hants, UK, 1-4

Schumacher, M., Forootan, E., van Dijk, A. I. J. M., Schmied, H. M., Crosbie, R. S., Kusche, J., & Döll, P. (2018). Improving drought simulations within the Murray-Darling Basin by combined calibration/assimilation of GRACE data into the WaterGAP global hydrology model. *Remote Sensing of Environment*, *204*, 212–228. https://doi.org/10.1016/j.rse.2017.10.029

Seo, K. W., Wilson, C. R., Chen, J. L., & Waliser, D. E. (2008). GRACE's spatial aliasing error. *Geophysical Journal International*, *172*(1), 41–48. https://doi.org/10.1111/j.1365-246X.2007.03611.x

Shen, Y., Chen, Q., & Xu, H. (2015). Monthly gravity field solution from GRACE range measurements using modified short arc approach. *Geodesy and Geodynamics*, *6*(4), 261–266. https://doi.org/10.1016/j.geog.2015.05.009

Swenson, S., Chambers, D., & Wahr, J. (2008). Estimating geocenter variations from a combination of GRACE and ocean model output. *Journal of Geophysical Research*, *113*(B8), B08410. https://doi.org/10.1029/2007JB005338

Taff, L. G. (1985). *Celestial mechanics: A computational guide for the practitioner*, (p. 540). New York: Wiley-Interscience.

Tapley, B. D., Bettadpur, S., Watkins, M., & Reigber, C. (2004). The gravity recovery and climate experiment: Mission overview and early results. *Geophysical Research Letters*, *31*, L09607. https://doi.org/10.1029/2004GL019920

Velicogna, I. (2009). Increasing rates of ice mass loss from the Greenland and Antarctic ice sheets revealed by GRACE. *Geophysical Research Letters*, *36*, L19503. https://doi.org/10.1029/2009GL040222

Velicogna, I., & Wahr, J. (2013). Time-variable gravity observations of ice sheet mass balance: Precision and limitations of the GRACE satellite data. *Geophysical Research Letters*, *40*, 3055–3063. https://doi.org/10.1002/grl.50527

Wahr, J., Swenson, S., Zlotnicki, V., & Velicogna, I. (2004). Time-variable gravity from GRACE: First results. *Geophysical Research Letters*, *31*, L11501. https://doi.org/10.1029/2004GL019779

Wang, C., Xu, H., Zhong, M., & Feng, W. (2015). Monthly gravity field recovery from GRACE orbits and K-band measurements using variational equations approach. *Geodesy and Geodynamics*, *6*(4), 253–260. https://doi.org/10.1016/j.geog.2015.05.010

Watkins, M. M., Wiese, D. N., Yuan, D. N., Boening, C., & Landerer, F. W. (2015). Improved methods for observing Earth's time variable mass distribution with GRACE using spherical cap mascons. *Journal of Geophysical Research: Solid Earth*, *120*, 2648–2671. https://doi.org/10.1002/2014JB011547

Watkins MM and Yuan DN (2014), GRACE JPL level-2 processing standards document for level-2 product release 05.1, GRACE 327-744 (v 5.1).

Wiese, D. N., Nerem, R. S., & Han, S. C. (2011). Expected improvements in determining continental hydrology, ice mass variations, ocean bottom pressure signals, and earthquakes using two pairs of dedicated satellites for temporal gravity recovery. *Journal of Geophysical Research*, *116*(B11), B11405. https://doi.org/10.1029/2011JB008375

Xu, P. (2008). Position and velocity perturbations for the determination of geopotential from space geodetic measurements. *Celestial Mechanics and Dynamical Astronomy*, *100*(3), 231–249. https://doi.org/10.1007/s10569-008-9117-x

Yuan D (2018) JPL level-2 processing standards document for level-2 product release 06. Technical report GRACE, 327–744.

Zehentner N and Mayer-Gürr T. Kinematic orbits for GRACE and GOCE based on raw GPS observations, Poster presented at the IAG Scientific Assembly 2013, 1.-6. September 2013, Potsdam, Germany

Zenner, L., Fagiolini, E., Daras, I., Flechtner, F., Gruber, T., Schmidt, T., & Schwarz, G. (2012). Non-tidal atmospheric and oceanic mass variations and their impact on GRACE data analysis. *Journal of Geodynamics*, *59*, 9–15.

Zhao, Q., Guo, J., Hu, Z., Shi, C., Liu, J., Cai, H., & Liu, X. (2011). GRACE gravity field modeling with an investigation on correlation between nuisance parameters and gravity field coefficients. *Advances in Space Research*, *47*(10), 1833–1850. https://doi.org/10.1016/j.asr.2010.11.041

Zhou, H., Luo, Z., Zhou, Z., Zhong, B., & Hsu, H. (2017). HUST-Grace2016s: A new GRACE static gravity field model derived from a modified dynamic approach over a 13-year observation period. *Advances in Space Research*, *60*(3), 597–611. https://doi.org/10.1016/j.asr.2017.04.026